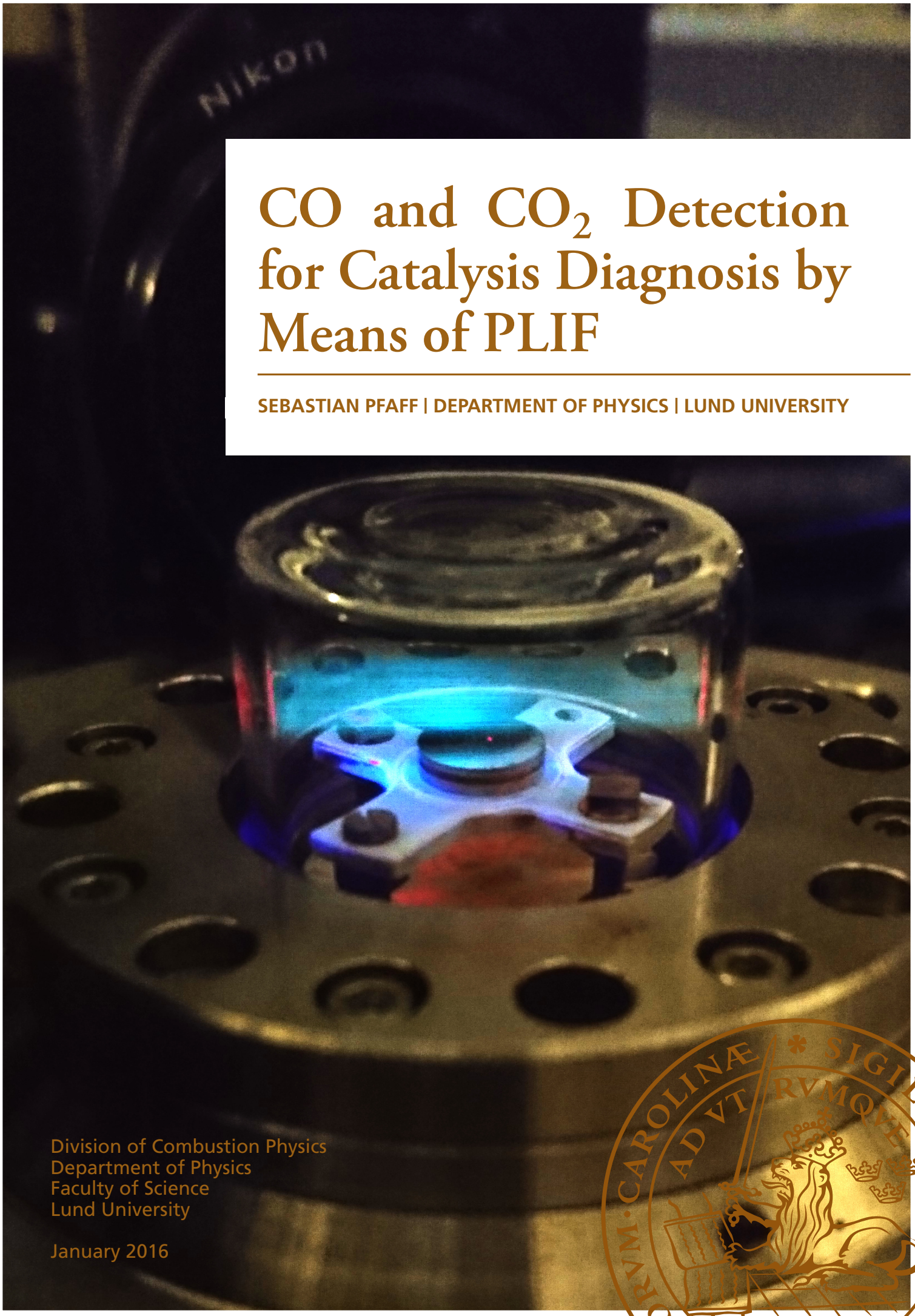


# CO and $CO_2$ Detection for Catalysis Diagnosis by Means of PLIF

SEBASTIAN PFAFF | DEPARTMENT OF PHYSICS | LUND UNIVERSITY

Division of Combustion Physics
Department of Physics
Faculty of Science
Lund University

January 2016

# CO and $CO_2$ Detection for Catalysis Diagnosis by Means of PLIF

Sebastian Pfaff


LUND
UNIVERSITY

A Thesis Submitted for the Degree of Master of Science
Supervised by Johan Zetterberg and Jianfeng Zhou
Project Duration: 9 Months

Division of Combustion Physics
Department of Physics
Faculty of Science

January 2016

18th January 2017

Lund Reports on Combustion Physics, LRCP-203
ISNR LUTFD2/TFCP-175-SE
ISSN 1102-8718

Sebastian Pfaff
Division of Combustion Physics
Department of Physics
Faculty of Science
Lund University
P.O. Box 118
S-221 00 Lund, Sweden

# Contents

## 0.1 Abstract

In order to fully understand the underlying processes of catalysis, it is vital to combine measurements of the catalyst surface, where the reaction occurs, with measurements of the gas concentration close to the catalyst.

We have developed a convenient setup, which uses a single laser system to visualise the gas surrounding a working catalyst *in situ* at realistic operating conditions. Planar Laser Induced Flouresence (PLIF) is a technique in which the gas to be detected is excited by a planar laser sheet. The subsequent fluorescence is then detected by a camera. With this technique, we are able to create accurate two-dimensional representations of CO and $CO_2$ concentrations, however, we think it will be possible to extend the list of gases in the future.

For $CO_2$ detection, we use an Nd:YAG laser to pump an OPO which had its idler output tuned to 2.7 µm. This beam was used to vibrationally excite the $CO_2$ molecules, after which they deexcite via a path that entails fluorescence at 4.26 µm. A focal plane array was subsequently used to image the fluorescence.

To detect CO, the same Nd:YAG laser is frequency doubled and used to pump a dye laser, the output of which is frequency doubled again and mixed with the residual beam left after the frequency doubling process. By tuning the dye laser, an output beam of 230.1 nm is obtained, which is used to excite CO using a two-photon transition. The fluorescence, which is in the visible range between 400 nm and 700 nm, is then deteced by an ICCD camera.

We have performed proof-of-concept measurements where the setup was used to image the gas surrounding a working Pd(110) single crystal catalyst. In these measurements, the catalyst temperature was ramped from 200 °C to 350 °C . CO and $CO_2$ were measured consecutively using similar temperature ramps. We found that we achieve detection limits of below 0.5 mbar for CO and below 0.1 mbar for $CO_2$ at temporal resolutions of 100 ms and spatial resolutions of 40 µm. The results of these measurements have resulted in a manuscript now submitted to *Applied Physics B*.

In addition, we have shown that it is possible and feasible to use the PLIF setup in conjunction with SXRD to perform simultaneous measurements of the catalyst surface structure and the surrounding gas. Clear correlations between a change in surface structure and changes in gas phase reaction products were found. Furthermore, we think this is the first time PLIF and SXRD have been used simultaneously.

## 0.2 Populärvetenskaplig sammanfattning

Katalysatorer påskyndar en reaktion utan att själva förbrukas; denna mening känner nog många igen från sin skoltid. Andra har hört talas om katalysatorer som något de "har i bilen". Mycket riktigt är det främst i bilar där vi i våra vardagliga liv stöter på katalysatorer. Här används de för att omvandla de mycket giftiga gaserna kolmonoxid och kväveoxid till för människorna ofarligt kvävgas och koldioxid. Kolmonoxid, alltså en molekyl med en kolatom och *en* syreatom ska alltså bli till koldioxid, en molekyl som består av en kolatom och *två* syreatomer. Det krävs alltså *en* enda ytterligare syreatom för att reaktionen ska kunna ske. Problemet är att det allmänt finns mycket få tillgängliga syreatomer, de flesta av dem har nämligen bildat molekyler av två syreatomer, par som sitter mycket hårt ihop. För att kunna använda syre från luften för att omvandla kolmonoxid till koldioxid måste syret alltså först delas upp.

De katalysatorer som renar bilarnas avgaser består av små metallkorn som är utspridda i ett skummgummiliknande medium. Den kemiska reaktionen som omvandlar gaserna sker på ytan av dessa metallkorn. Det går att tänka sig metallytan som en yta täckt av utstickande kilar. När en syremolekyl, alltså två syreatomer som sitter ihop, sätter sig på ytan, trycker kilarna isär syremolekylen så att de två syreatomerna skiljs och till slut ligger enskilda på ytan. Detta gör det enkelt för kolmonixidmolekylerna att plocka upp en av syreatomerna och bli till koldioxid.

För att kunna vidareutveckla och förbättra katalysatorerna krävs givetvis en utökad förståelse för vad som sker på ytan, ända ner på atomnivå. Processen må verka enkel, men detaljerna kring de underliggande mekanismerna är fortfarande föremål för spekulation. För att gå till botten med detta krävs tekniker för att undersöka ytornas struktur på atomnivå. Dessa tekniker måste givetvis kombineras med tekniker som undersöker hur gasfördelningen runt katalysatorn förändras, på så sätt kan förändringar i ytstrukturen kopplas till gasomvandlingsprocessen. Det finns alltså ett intresse att vidareutvecka tekniker med vars hjälp det är möjligt att noga undersöka gaskoncentrationer och gasfördelningar.

Många har säkert märkt att en gitarr- eller pianosträng kan börja vibrera "av sig själv" när den utsätts för ljud av rätt frekvens, strängens resonansfrekvens. När den då vibrerar avger den återigen ljud av denna frekvens. På samma sätt har atomer och molekyler resonansfrekvenser; om partiklarna utsätts för ljus av rätt färg, alltså rätt frekvens, kommer de ta upp ljuset och därefter åter sända ut det. Detta fenomen kallas fluorescens.

Varje gas, som ju består av molekyler eller atomer, har sina egen resonansfrekvenser vid vilka gasen fluorescerar. Detta fenomen utnyttjas i tekniken "Planar Laser Induced Fluorescence", förkortat PLIF. Tekniken går ut på att skjuta en laserstråle genom en gasblandning. Laserns färg är inställd att matcha resonansfrekvensen för en av gaserna i blandningen. Detta får just den gasen att lysa, vilket gör att man med en kamera kan ta bilder som visar var just den gasen finns, en mycket användbar teknik för att undersöka hur gasblandningen runt en katalysator ser ut.

Vi har vidareutvecklat denna teknik och visat att det är möjligt att kombinera den med andra metoder som gör det möjligt att studera ytors struktur på atomnivå.

Genom att vidareutveckla tekniker som PLIF kan vi lära oss mer om, och på sikt förbättra, katalysatorer i framtiden, något som inte bara är viktigt för bilindustrin; nästan alla kemiska processer som används för att skapa produkter som vi nyttjar i vår vardag tar nytta av katalys på ett eller annat sätt. I vissa fall hade processerna inte varit möjliga utan katalys, i andra fall hade de förbrukat mer energi eller skapat större mängder skadliga avfallsprodukter. Att vidare arbeta på att utveckla katalysatorer är därför essentiellt för att kunna fortsätta att förbättra vår levnadsstandard och vår miljö.

## 0.3 List of Abbreviations

**CMOS** Complementary Metal Oxide Semiconductor

**CTR** Crystal Truncation Rod

**DESY** Deutsches Elektronen-Synkrotron

**FPA** Focal Plane Array

**ICCD** Intensified Charge-Coupled Device

**IF** Interference Filter

**IR** Infrared

**LCAO** Linear Combinations of Atomic Orbitals

**LEED** Low Energy Electron Diffraction

**LIF** Laser Induced Fluorescence

**LV** Leak Valve

**MS** Mass Spectrometer

**Nd:YAG** Neodymium doped Yttrium Aluminium Garnet

**OPO** Optical Parametric Oscillator

**PC** Pressure Controller

**PG** Pressure Gauge

**PID** Proportional-Integral-Derivative

**PLIF** Planar Laser Induced Fluorescence

**PMT** Photomultiplier Tube

**SHG** Second Harmonic Generator

**STM** Scanning Tunnelling Microscopy

**SXRD** Surface X-Ray Diffraction

**UHV** Ultra High Vacuum

**UV** Ultra-violet

**XPS** X-Ray Photoelectron Spectroscopy

**XRD** X-Ray Diffraction

# 1 Introduction

From the cleansing of automotive exhausts to the production of pharmaceuticals and fertilizers, catalysts are today ubiquitous in the industrialised world; without them our current standard of living could impossibly be maintained. Catalysis is also a part of many chemical reactions used to decompose harmful waste products, such as the carbon monoxide and nitrogen oxides from car exhausts, or the waste products from chemical industries. This makes catalysis an important tool for environmental protection. As such, it is of utmost importance to further improve our understanding of the underlying processes in order to develop and streamline catalysts on both the microscopic and the macroscopic scale.

Catalysis was first described in 1835 by Berzelius [1, 2] who described the "catalytic force" as an unknown force exercised upon the reactants by the catalyst. Since then, much research has gone into investigating the details involved in catalytic processes. The catalytic processes involved in cleaning car exhausts mentioned above represent so called heterogeneous catalysis, where the catalyst is a solid, often metal, while the reactants are either gases or liquids. Here the catalytic reactions take place on the surface of the solid, which calls for a deeper understanding of surface structures if the working principle of catalysts is to be fully understood [3]. Especially from the 1970s and onwards, many techniques suited to study surface structure have been developed that rapidly accelerated our knowledge on heterogeneous catalysis. One example is Scanning Tunnelling Microscopy (STM) [4], where a voltage is applied between a surface and an atomically sharp tip scanning over the surface, while the tunnelling current is measured. Electron based techniques such as X-ray photoelectron spectroscopy (XPS) [5], or Low Energy Electron Diffraction (LEED) [6] have also proven very useful to further our understanding of surface based processes.

The downside of many of these electron based techniques is their reliance on ultra high vacuum (UHV) to function, as the mean free path of electrons in air is extremely short. Consequently, these otherwise excellent techniques cannot be employed in realistic catalyst operating conditions, which usually involve pressures of around 1 bar or above. Hence, there is a pressure gap of nine orders of magnitude which has to be bridged using alternative techniques. There has been progress in making electron based methods available at higher pressures with techniques such as high pressure XPS (HP-XPS) [7, 8]. With this technique, an evacuated, cone shaped, nozzle is lowered over the sample to be studied in an attempt to minimize the path that the electrons have to spend travelling though high pressure. However, even these techniques only allow for pressures up to a few mbar before the signal to noise ratio becomes too low. Also, variants of STM that allow measurements at high pressure have been recently developed [9]. These measurements show radical changes in catalyst properties, such as completely different surface structures, when the catalyst is exposed to higher pressures [10]. Therefore, there is interest to study the active catalyst surface at realistic operating conditions. In addition to these techniques, there have also been developments in the field of Surface X-Ray Diffraction (SXRD), yet another surface technique not requiring UHV, which could be used to investigate the surface structure of active catalysts [11].

Although only measuring the surface structure does often not give the full picture; a variation of surface structure must be matched with a change in reactant and product concentrations if any conclusions about actual catalyst activity are to be drawn. Traditionally, mass spectrometers (MS) have been used to measure the gas concentration near an active catalyst to gauge its effect. However, most commonly the MS is set up in such a way that it measures an average of the gas in the reactor. If one is interested in the gas distribution at the catalyst surface, the only way to measure this is by pla-

cing a tube or orifice right above the catalyst [12]. This might disrupt the flow around the catalyst, and is difficult to combine with other experimental surface techniques. Moreover, the distance between the tube inlet and the actual analyser often results in a delay of the concentration signal.

Planar laser induced fluorescence (PLIF) is an alternative, laser-based technique which allows for fast, spatially resolved measurements of a gas distribution [13, 14]. As with most laser based techniques, PLIF is also non-intrusive; no probes or tubes have to be placed in close proximity to the catalyst surface allowing for *in situ* measurements. This also means that PLIF can be used in conjunction with surface techniques, such as SXRD, to visualize the response of the gas phase to measured surface fluctuations, as nothing will obstruct the sample.

Traditionally, the technique was mainly used for flame studies, for example major and minor species concentration, flame temperature and flame velocity [14]. In the field of catalysis research, PLIF is not as commonly used. Though, the technique has been used to detect the formation of OH during $H_2$ oxidation using a Pt catalyst [15, 16, 17]. It has also been used to probe the desorption rate of OH from a Pt catalyst during the catalytic water formation reaction [18].

More recently, PLIF has been used to observe the gas phase during oxidation of CO to $CO_2$ using platinum group metal catalysts [19, 20]. To that end, two separate, rather cumbersome laser systems were employed for the detection of both reaction species. This setup is difficult to use in conjunction with surface techniques such as SXRD because it is complicated to move and does not fit easily inside a cramped synchrotron end station.

In this thesis, we have developed a more convenient PLIF setup, where both CO and $CO_2$ are detected using the same laser system. This smaller setup was then used to perform simultaneous measurements with PLIF and SXRD at PETRA III, a synchrotron at DESY (Deutsches Elektronen Synkrotron). These measurements indicated clear correlations between the catalysts surface structure and a change in gas constituents. To our knowledge, this is the first time such simultaneous measurements have been performed. In addition, a proof-of-concept measurement was performed to demonstrate the temporal and spatial resolutions of the technique.

# 2 Theoretical Background

## 2.1 Lasers

In this section I will briefly outline the theory behind the optical devices used to generate the various frequencies of light used for CO and $CO_2$ detection with PLIF.

A laser is a device, which generates monochromatic, coherent and intense light. It consists of an optical cavity and a lasing medium [21]. The laser medium is chosen to consist of a solid, liquid or gas, which has energy levels with spacings and lifetimes to allow for population inversion. This state, where the electron population of a higher energy level is greater than that of a lower level, can be archived by heavy optical pumping. The pumping may be performed by, for example, a high intensity flash lamp or another laser. When population inversion is achieved, a photon originating from a de-excitation of an atom or molecule in the laser medium may, through stimulated emission, move another atom or molecule in the laser medium to a lower state, creating an additional photon with the same phase and wavelength. The original light is thus amplified by stimulated emission. Since this process causes a chain reaction, a large amount of high intensity, coherent light is created.

Without the cavity, this light may consist of multiple frequencies depending on the available transitions in the laser medium. However, the length of the cavity containing the laser medium is chosen to match the resonance condition of the desired frequency, which ensures that only this particular frequency is amplified.

If the laser is constructed in such a way that all accumulated population inversion is released at once in short bursts, we consider the laser to be pulsed. This way, pulses of extremely high intensity may be created. In the case of the Neodymium-doped Yttrium Aluminium Garnet (Nd:YAG) laser used in this work, a so called Q-switch was used to create the pulses, which resulted in pulses that were a few nanoseconds long and around 1 J in energy, yielding gigawatt peak power.

These short, highly energetic pulses are used to utilize so called non-linear processes. Non-linear processes make it possible to obtain higher order harmonics of the incident light frequency, effectively doubling or tripling it. It is also possible to combine two beams in such a way that their frequencies are added or subtracted.

To understand these processes, we can look at the polarisation $P$, which a material experiences when exposed to an electric field $E$ given by [22]

$$P = \chi_1 E + \chi_2 E^2 + \chi_3 E^3 + \dots \,, \tag{1}$$

where the coefficients $\chi_i$ are the susceptibilities telling how easily a material is polarised. The higher order coefficients are typically very small, however if $E$ is sufficiently large, the second-order term may be exploited.

Assuming the electric field is a plane wave with frequency $\omega$, by simple trigonometry we can see that the second order polarisation $P_2$ gives rise to a cosine term with a frequency of $2\omega$.

$$P_2 = \chi_2 E_0^2 \sin^2 \omega t = \chi_2 E_0^2 \left( \frac{1 - \cos 2\omega t}{2} \right) \tag{2}$$

Similarly, by substituting a sum of two waves with different frequencies $\omega_1$ and $\omega_2$ into $E$, it can be shown that a term with a frequency corresponding to the sum $\omega_1 + \omega_2$ or the difference $\omega_1 - \omega_2$ of the initial frequencies may be obtained. These principles are used in the second harmonic generator (SHG) and frequency mixing crystals in the experimental setup.

Another component is a dye laser. Here, a dye with a very broad spectrum is used as laser medium. This dye is in turn excited by pumping it with another laser. Since a specific cavity length will allow only a very small range of frequencies to resonate, a specific frequency may be chosen within a small range by controlling the cavity length. This length adjustment is often performed using a rotatable grating acting as one of the cavity mirrors.

## 2.2 Molecular Spectra

In order to understand which transitions are suitable for PLIF, one must first understand the peculiarities of molecular spectra. In this section I will thus briefly treat the theory behind molecular spectra, as well as explain the at times confusing notation used to denote molecular energy levels. For simple molecules, the most common way to construct a model for the energy levels is using so called linear combinations of atomic orbitals (LCAO) [22]. This means that for every pair of atomic orbitals, a pair of molecular orbitals is created, one by adding the wavefunctions representing two atomic orbitals, the second by subtracting one from the other.

As carbon monoxide is a diatomic molecule, it serves as a great example. Figure 1 shows an energy level diagram of CO. The electronic ground state is always labelled $X$. This state corresponds to all electrons being in the lowest possible orbitals. As the total orbital angular momentum of all electrons involved in this state is zero, the orbit will be a $\Sigma$ state (analogous with $s$ for atoms). The excited states of the same multiplicity as the ground state are labelled $A$, $B$, and so on, while excited states of a different multiplicity are labelled $a$, $b$ and so on. Since the $A$ state implies one electron moving to a higher, previously empty orbital which happens to be originating from the atomic $2p$ states, that state will have a total angular momentum of one, which means it will be a $\Pi$ state (analogous with $p$ for atoms).

Since a molecule is not spherically symmetric, it may be vibrationally or rotationally excited. It has been shown (Born-Oppenheimer approximation) that these excitations may be treated separately from the electronic excitations, since the much heavier nuclei, which give rise to vibrational and rotational levels move much slower than the light electrons, due to their difference in mass. [24]. We can thus assign vibrational states to each electronic state; the labelling scheme used for vibrational states is rather simple, vibrational states of the ground state are labelled $v' = 0, 1, 2, ..., n$ whereas vibrational states of excited states are labelled $v'' = 0, 1, 2, ..., n$.

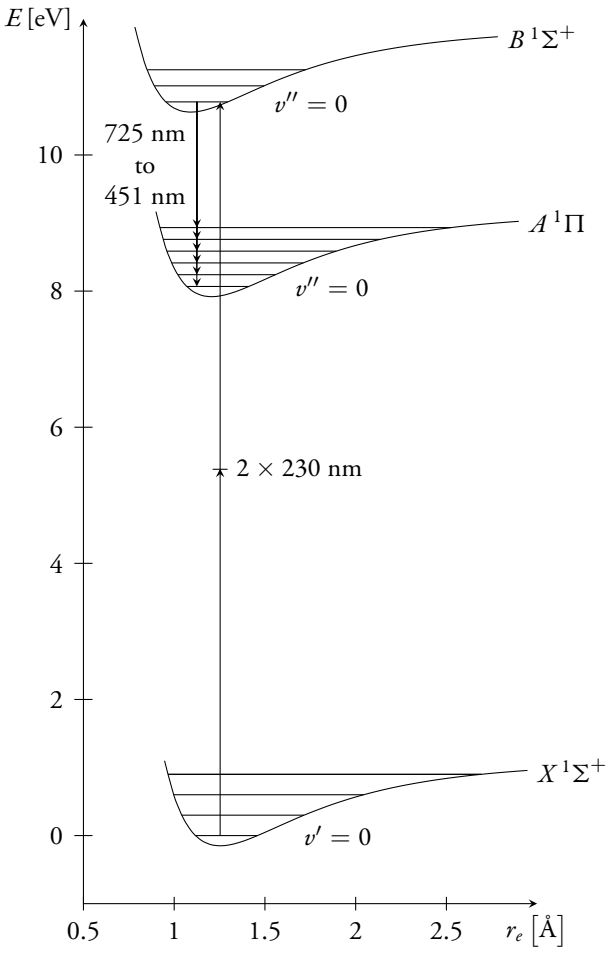


***Figure 1:*** *A energy-level diagram showing the states and transitions involved in the two-photon excitation process. The shape of the potentials is arbitrary. Created using data from [23].*

Triatomic molecules have vibrational modes similar to the thee vibrational modes of three coupled oscillators, hence there are three vibrational quantum numbers, $v_1$, $v_2$ and $v_3$ which specify these modes. In addition to this, the states may have an angular momentum denoted $\ell$. Vibrational states of triatomic molecules are then referred to using $(v_1\, v_2^{\ell}\, v_3)$, for example $(10^01)$.

The transitions of interest to this work, which are used to excite CO and $CO_2$ for subsequental detection using PLIF as explained in the next section,

are shown in figures 1 and 2.

For CO, the two-photon excitation scheme presented is used for PLIF due to the rather easy accessibility of the 230.1 nm wavelength in addition to the easily detectable fluorescence, which conveniently is in the visible range. Detection of CO using vibrational transitions excited by an IR laser is certainly also possible [25]. However, it is problematic in conjunction with presence of $CO_2$ because energy transfer from CO to $CO_2$ may occur.

Regarding the choice of excitation scheme for $CO_2$ detection, it must first be concluded that a vibrational transition must be chosen as no suitable transitions are available in the visible or UV range. As to the choice of which vibrational transition to target, the target transition needs to have a large enough cross section to excite a sufficient number of atoms. However, if the cross-section is too large, a substantial amount of the laser beam energy will be lost due to absorption by $CO_2$ in the air before the beam even reaches the reaction cell. In this regard, the 2.7 µm transition mentioned is a good compromise. It would be possible to target the $(00^01)$ state using a transition at 4.26 µm directly; though it has precisely the problem of being absorbed by the $CO_2$ in the air before reaching the reaction cell. The only alternative is then to purge the entire beam path with another gas such as nitrogen. While this is indeed possible, it would add a further layer of complication to the optical setup.

## 2.3 Planar Laser Induced Fluorescence

In Laser Induced Fluorescence (LIF), a laser beam is used to excite the molecules to be detected. As the gas later decays to a lower state, photons are emitted, which may be detected in a number of ways. Traditionally, simple one-dimensional detectors such as photomultiplier tubes (PMT) are used [26]. However, it is possible to extend this and use two-dimensional detectors such as Intensified Charge-Coupled Devices (ICCD) in conjunction with a laser beam formed into a planar sheet,

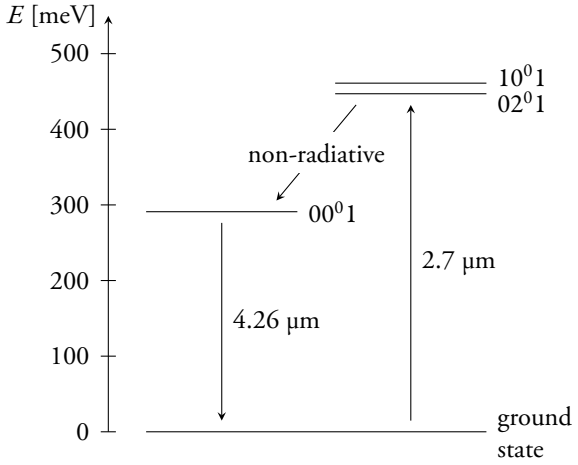


***Figure 2:*** *Excitation scheme for $CO_2$ showing the transitions of importance to this work. Created using data from [23].*

yielding spatially resolved images of the gas distribution in the cell [20]. This two-dimension technique in then referred to as Planar Laser Induced Fluorescence (PLIF) [14].

In order to detect the presence of a gaseous species using PLIF, a suitable target transition needs to be chosen. This can be either an electronic transition usually in the visible or UV regime or a vibrational transition using in the IR regime.

In an attempt to find an expression for the total intensity at a given gas pressure, we begin by looking at the number of gas molecules per volume of ideal gas. The ideal gas law yields

$$\frac{P}{k_B T} = \frac{N}{V} \,, \tag{3}$$

where $N/V$ is the number of gas molecules, in a given volume, $k_B$ is the Boltzmann constant, $P$ the gas pressure and $T$ the gas temperature. Now, as a laser passes through a gas of molecules, there will be fluorescence from the deexcitations of molecules excited by the laser. An approximation of the fluorescence intensity $I$ may then be given by something along the lines of [20]

$$I = c_e E \sigma_0 \int g(\nu)\sigma(\nu)\,\mathrm{d}\nu \cdot f(T)\,\frac{P}{k_B T} \cdot Q\alpha \,, \tag{4}$$

where $c_e$ is the camera photon detection efficiency, $E$ is the incident laser energy, $\sigma_0$ is the photon interaction cross-section of the target species, $g(\nu)$ is the laser lineshape, $\sigma(\nu)$ is the target species lineshape, $f(T)$ is the fraction of electrons in the lower state of the targeted transition, $P/k_BT$ is the number of molecules to interact with, as discussed above, and $Q$ is the photon quantum yield or quenching term.

We will now examine the equation and look at each of the terms in more detail. First we have the camera photon detection efficiency $c_e$ which represents the fraction of photons reaching the camera that are actually registered. This term depends on the camera model, optics, and possibly also on the wavelength. This would not be an issue for us as we assume the incident wavelength distribution to be independent of our experimental parameters. As long as the camera is not saturated, the term should not depend on the number of incident photons, which means it should not alter the linearity of the equation.

Next we have the energy term $E$ that specifies the laser energy, which we assume to be proportional to the number of photons given a fixed wavelength. It is reasonable to assume that the number of excited atoms will be proportional to the number of photons given that the targeted transition is not a two-photon transition as is the case with CO detection. In such a case this term would instead be $E^2$.

The integral term represents the overlap between the laser line shape and the absorption spectrum of the species to be investigated. A good alignment of the two, which corresponds to a large value of the integral, is absolutely critical to obtain a large fluorescence signal yield. Its implications on this work will be discussed in the results section.

Moving on, the Boltzmann fraction term $f(T)$ is mainly relevant for the population of vibrational states of the electronic ground state, as this usually is the lower level of the targeted transition. If the laser linewidth is small, electrons populating the first or second vibrational levels might not be excited by the laser, which decreases the signal. The effects of this term for $CO_2$ and CO are shown in figure 3. For $CO_2$, the lowest vibrational energy state is at 83 meV [23], which means ground state depopulation has a rather large effect on the overall signal at higher temperatures. On the other hand, CO has its lowest vibrational state at around 248 meV [23] meaning that thermal excitations have a very limited effect.

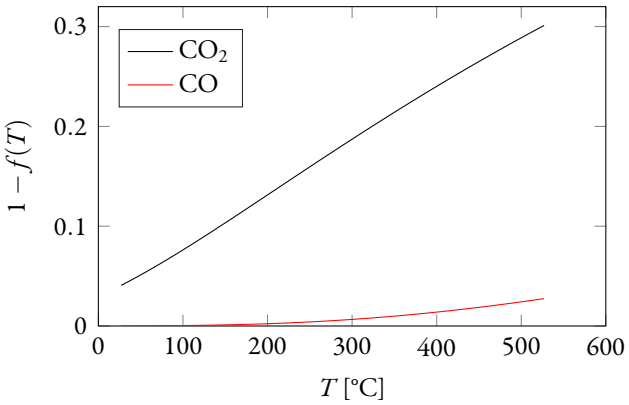


***Figure 3:*** *The ground state depopulation as result of thermal excitations to other vibrational states for CO and $CO_2$.*

Furthermore, we have the quenching term $Q$, which specifies the fraction of excited atoms or molecules actually deexciting through photon emission of the desired wavelength. Other processes may be vibrational or rotational energy transfer to another atom or molecule of the same or another species. The atom or molecule may also simply decay to a lower but still excited vibrational state before decaying to the ground state. These processes are difficult to theoretically formulate, but it is possible to perform measurements to gauge their effect. While such measurements were performed within the scope of this thesis, an attempt will be made to discuss their effect on the results in the discussion section.

$\alpha$ represents losses through reabsorption of photons by another atom or molecule of the species to be detected. This simply follows the Lambert–

Beer law, which states the fraction of available photons that is absorbed per unit length [27]. This results in an exponential decrease in intensity as given by

$$I = I_0 \mathrm{e}^{-\sigma_0 N \ell} \ , \tag{5}$$

where $I$ is the light intensity after travelling a distance $\ell$ through a medium with absorption cross section $\sigma_0$ and density $N$, if the initial intensity at $\ell = 0$ is $I_0$. This effect can be minimized by minimizing the path that the fluorescent light travels through gas containing the species to be detected, for example by placing the detector close to the fluorescence source or by purging the path with a different gas. However, these measures do not mitigate the effect of self-absorption within the cell. The effect from this will be further discussed in the discussion section.

Altogether, non-linear effects such as self-absorption are minimal, which means that the recorded LIF intensity is mainly dependent on temperature and gas pressure. If the temperature dependence can be efficiently compensated, which is indeed possible, the PLIF signal will be linearly dependent on the gas pressure of the species to be measured. PLIF is thus an excellent technique to non-intrusively determine gas concentrations.

## 2.4 Catalysis

In this section, I will discuss the concepts of catalysis, focusing on the process of CO oxidation to $CO_2$ according to

$$2\mathrm{CO} + \mathrm{O_2} \rightarrow 2\mathrm{CO_2} \ ,$$

as well as the metal catalysts used to catalyse the reaction.

A catalyst is a substance, which lowers the activation energy of a chemical reaction without the substance itself being consumed or altered. If the catalyst and the reactants are not in the same phase, the catalytic process is referred to heterogeneous catalysis. The most common examples of this are gases or liquids reacting with a solid catalyst. In a heterogeneous catalytic process, the reactants first need to be adsorbed on the surface of the catalyst. Here they react, after which the reaction products must desorb from the surface, in order for the same surface area to be used again. The reaction path of a catalysed process is visualised in figure 4. Note that even with a catalyst present, a certain activation energy is necessary for the reaction to occur, which is usually supplied by heating the catalyst.

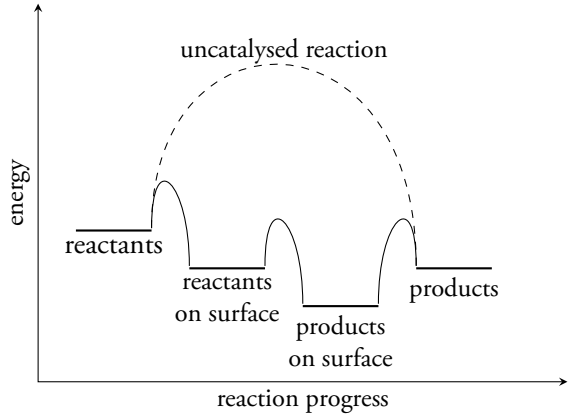


***Figure 4:*** *Schematic diagram of a heterogeneous catalytic process. The dashed line shows the flow of the reaction without a catalyst while the solid lines show the reaction steps with a catalyst involved.*

As mentioned, the catalysed reaction in heterogeneous catalysis must contain some type of adsorption of the gaseous reactants on the surface. This may occur in a number of ways, where different physical effects yield the potentials that hold the adsorbants in place [28]. As a gas molecule approaches a metal surface, it will first feel an electromagnetic attraction. This is can be understood by looking at the conceptual image charge, by which the electric field from a point charge near a surface may be understood. As the electron cloud around the gas molecule is never completely homogeneous, a small residual charge will always remain that will result in an attraction towards the equal and opposite image charge inside the metal. This force is often referred to as van der Waals force. If this attractive force is sufficiently large, the molecule may stick to

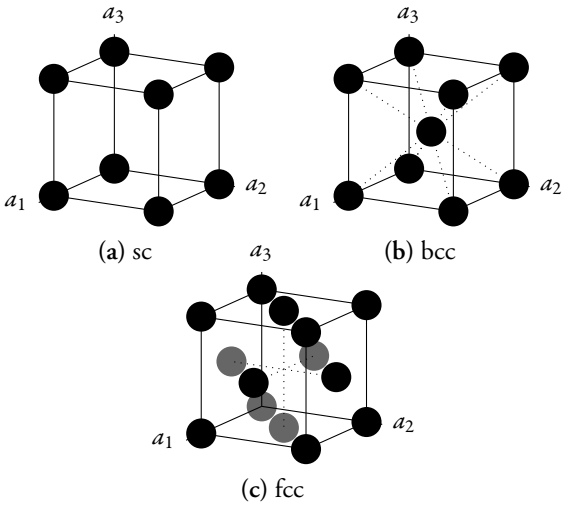


***Figure 5:*** *Examples of three possible metal crystal structures: Single cubic (sc), body centred cubic (bcc) and face centred cubic (fcc).*

the surface at a distance where the attractive force is equal to the Pauli repulsion force. This rather weak form of adsorption called physisorption.

If the molecule is close to the surface and of a suitable species, chemical reactions may occur causing the adsorbant to stick to the metal surface by means of chemical bonds with metal atoms. However, initially the intermolecular bonds of the gas molecule are still in place. This process is referred to as chemisorption. Given the right surface structure the intermolecular bonds may be weakened, which may cause them to break and the molecule to dissociate with very little external energy supplied. Consequently, the individual constituents of the initial gas will be individually bound to the surface.

If now another gaseous molecule, which may form an even stronger bond with one of the individually adsorbed gas constituents, approaches and adsorbs to the surface, it may bind to one of the atoms on the surface forming the reaction product. The product then desorbs and leaves the surface.

In case of the reaction discussed in this thesis, CO oxidation to $CO_2$, the adsorbant will be $O_2$. The $O_2$ molecule will disassociate as it binds to the surface, given that a little energy is supplied in the form of heat. CO molecules may now pick up the individually surface bound O atoms to form $CO_2$.

Consequently, the surface structure is of importance and will influence the adsorption abilities of the catalyst surface. To understand how crystal surfaces form and how they can be altered, we must first look at the crystal structure of metals. When discussing crystal structures, one usually looks at the smallest volume which, when repeated, will form the whole crystal. This volume, which is referred to as the primitive unit cell of the crystal, may look different depending on the material; it may be based on a cubic pattern, or based on more complicated shapes such as hexagons. The most simple cubic structure is the simple cubic (sc) structure in which one atom is in every corner of the unit cell as shown in figure 5a. More complicated cubic crystal structures include body-centred-cubic (bcc) and face-centred-cubic (fcc) as shown in figure 5b and 5c respectively. Thus, by specifying the crystal structure type together with the lattice parameters $a_1$, $a_2$ and $a_3$, which signify the interatomic distances along the $x$, $y$, and $z$ axes, the entire crystal structure can be defined.

By cutting crystals along different planes, many different surface structures can be created from a single crystal structure. To define how surface structures are cut, it is sensible to introduce the concept of Miller indices first proposed by William Hallowes Miller in 1839 [29]. Miller indices are constructed by finding the intersections of the cutting plane with the $x$, $y$, and $z$ axes. The reciprocals of the intersection position along the axes are then give the Miller indices of that cut. A few examples are given in figure 6. In a), the surface is a (110) surface as the cutting plane intersects with the $x$ and $y$ axes at 1, whereas it never crosses the $z$ axis which may be thought of as the surface intersecting with the $z$ axis at an infinite distance. Taking the reciprocal gives $(1^{-1}\ 1^{-1}\ \infty^{-1})$ or (110). In d), the (201) surface is shown which intersects with the axes at ½, $\infty$ and 1. Note that two surfaces are drawn in some

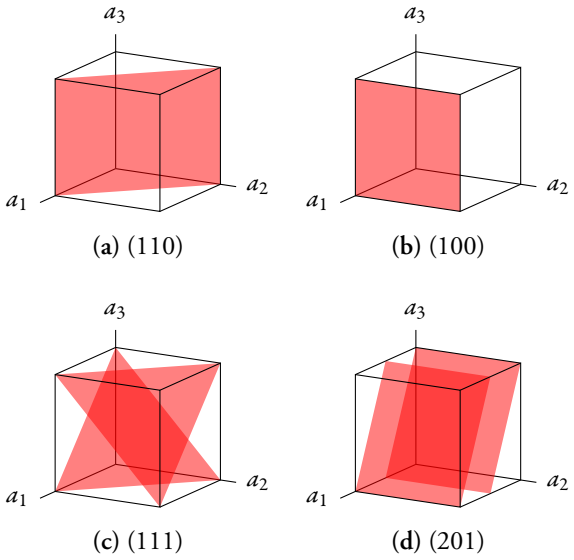


***Figure 6:*** *A number of unit cells with cuts yielding surfaces with various Miller indices marked in red.*

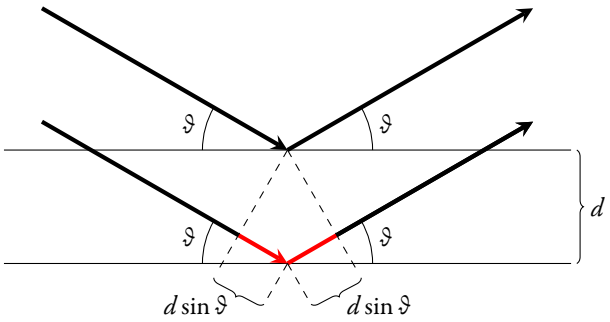


***Figure 7:*** *Braggs Law. Rays reflected by the lower reflector will have travelled further as indicated by the red lines. If the angle is such that positive interference is achieved between rays reflected by different layers, a bragg spot will appear.*

of the figures, where one is simply the continuation of the previous in an adjacent unit cell.

For the oxidation of CO to $CO_2$, one usually chooses platinum-group metals such as Palladium (Pd), Rhodium (Rh) or Platinum (Pt). These metals successfully disassociate $O_2$ while still releasing the reaction products at a high rate to free the used active sites. For model catalysts such as those used in this work, the metal is cut and polished to exhibit the specific surface structure, which is to be used as active surface during catalysis. In this thesis, the catalysts used are Pd(100) single crystals.

## 2.5 X-Ray Diffraction

X-Ray Diffraction (XRD) is a technique used to study the atomic structure of both bulk and surface matter. One great advantage of XRD, when applied in the field of heterogeneous catalysis, is the possibility to study the surface-gas border at higher pressures, something not easy with traditional surface techniques involving electrons such as XPS or LEED.

XRD involves shooting an X-ray beam at the sample to be investigated while examining the intensity distribution of the diffracted beams. If the sample has some sort of regular structure as is the case in crystals, the incident rays will be reflected at regular intervals. Figure 7 shows the principle behind this. The incident X-rays are reflected by some regular feature with spacing $d$ of the sample, represented by horizontal lines. These regular features could be the layers of atoms in a crystal often referred to as crystal planes. As can be seen, the additional distance that the beam has to travel, if it is instead reflected by a plane further into the sample, is $2d \sin \vartheta$, where $\vartheta$ is the incident angle of the X-rays. If the wavelength of the X-rays is $\lambda$, constructive interference between reflected beams originating from consecutive crystal planes will occur if the difference in path length is one wavelength or an integer multiple thereof. This yields the so called Bragg's law which states that bright diffraction spots will appear according to

$$2d \sin \vartheta = n\lambda. \tag{6}$$

From this equation, it is evident that smaller interplanar distances must yield larger diffraction angles in order for the equality to be fulfilled given a fixed wavelength.

In order to better understand how the spacing of the diffraction spots relates to the crystal

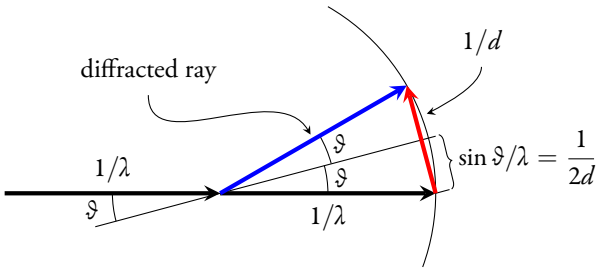


***Figure 8:*** *An attempt to explain why XRD gives rise to interference maxima at the reciprocal of lattice distances. The variables $d$ and $\vartheta$ represent the same distance and angle as they do in figure 7*

plane distance in the lattice, we may introduce the concept of an Ewald sphere, first introduced by Paul Ewald in 1913 [30]. This concept is illustrated in figure 8. We consider the incident X-ray beam as a wave vector with length $1/\lambda$ hitting the sample in the middle of a sphere of the same radius at an angle $\vartheta$. The angle between the continuation of the original beam and the beam pointing towards the first diffraction maximum will then be $2\vartheta$, as shown in the figure. We can thus, using simple geometrical arguments, conclude that the distance between the intersection of the sphere with the continuation of the incident beam and that of the reflected beam will be $1/d$. This in turn means that every distance between crystal features in the real crystal will be represented by a spot at the reciprocal of that distance. As such, the diffraction pattern will be the Fourier transform, a mathematical description of the frequency constituents, of the sample lattice structure. With this knowledge, the crystal structure of the sample can be accurately determined.

So far we have only treated XRD as a technique to investigate the properties of bulk crystals, but as mentioned earlier, it is also possible to use XRD as a technique to investigate the surface structure of a crystal. When used in such a way, the technique is referred to as Surface X-Ray Diffration (SXRD). Of course, a part of the diffraction signal from a given sample will always be from atoms at or very near the surface. However, due to the large penetration depth of X-rays in most matter, most of the signal will be originating from bulk structure. This issue can be alleviated by choosing a very shallow incident angle between the X-rays and the sample surface. In doing this, the X-rays will pass through a large number of surface or near-surface atoms before it enters the bulk, yielding a large increase in surface orienting from the surface.

The characteristics of a SXRD signal are so-called Crystal Truncation Rods (CTR). The origin of these is visualised in figure 9. As discussed earlier, the diffraction pattern will be the Fourier transform of the actual crystal structure, which corresponds to a frequency map of that structure. For an infinite, regular bulk crystal, the frequency constituents will be well defined as the reciprocal distance between the bulk atoms. This is easy to understand: If for instance, you walk along an infinite fence at a speed of 1 $\mathrm{ms}^{-1}$, and the spacing between the fence poles is 3 m, the frequency at which you will pass the poles will be ⅓ poles per second.

As soon as the crystal is truncated, there is no longer a well defined frequency. Instead, one can show that by adding a large number of oscillating functions of different frequencies, it is possible to construct rather sharp edges. Therefore, as a crystal is truncated, the originally sharp points in the diffraction pattern, which correspond to discrete frequencies, will be smeared out to form rods. These rods are a typical characteristics of an SXRD signal. By analysing the intensity distribution along the rods, one may draw conclusions about the details of the surface. However, such discussion is beyond the scope of this thesis, for further details, refer to e.g. [31].

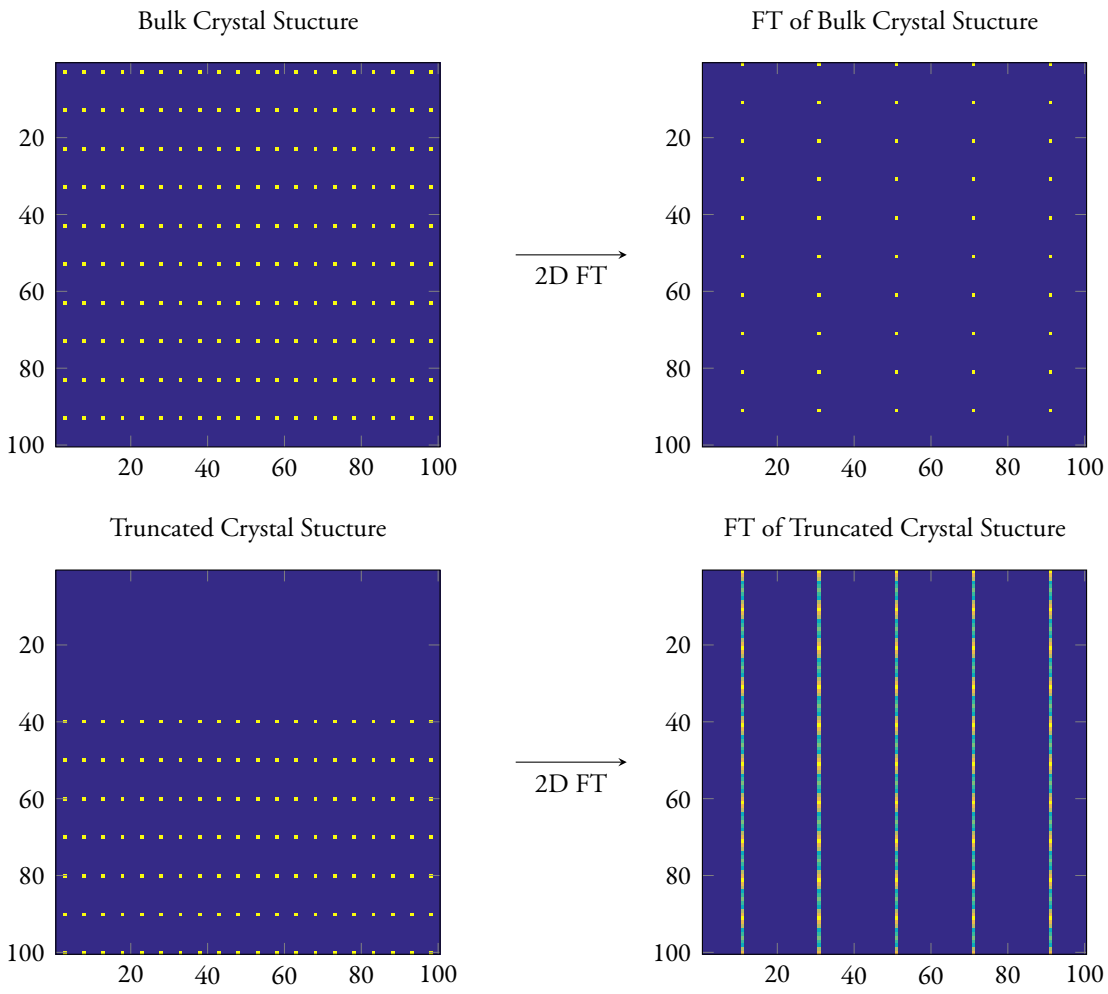


***Figure 9:*** *The origin of crystal truncation rods. The images to the left represent a crystal lattice, the right images the respective 2D Fourier transform.*

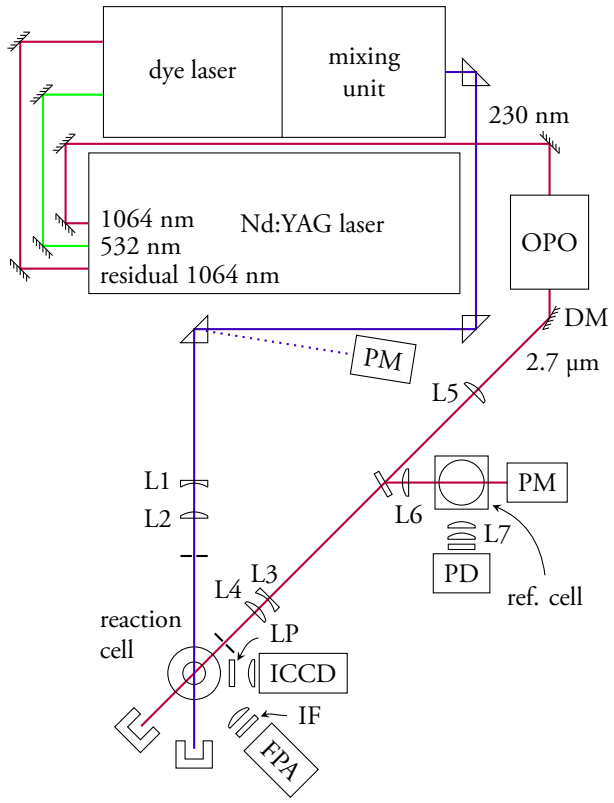


***Figure 10:*** *Schematic view of the lasers and related optics used for both $CO_2$ and CO detection.*

# 3 Method

In this section, I will explain the experimental methods used within the scope of this thesis. I will begin by presenting the lasers and optical setup used for detection of CO and $CO_2$. I will then move on to the auxiliary systems, such as the gas flow apparatus and the reaction cell. Finally, I will explain the post-processing steps required to create the final concentration maps from the raw data.

## 3.1 Planar Laser Induced Fluorescence

For the main experiment the optics were set up as presented in figure 10. A photograph of the same setup is shown in figure 11. An Nd:YAG laser (Continuum Powerlite DLS 8000) with a fundamental output at 1064 nm was used as the main light source. This laser operates in Q-switched pulsed mode at 10 Hz with a maximum per-shot energy of 1 J and a pulse length of 6-8 ns. This laser was then used to pump either an optical parametric oscillator (OPO, GWU-Lasertechnik OPO-S-1064) for $CO_2$ detection or a dye laser (Continuum Vista) for CO detection as explained below.

### 3.1.1 Carbon Monoxide Detection

CO was detected by exciting a two photon transition from the $X\,^1\Sigma^+$ to the $B\,^1\Sigma^+$ electronic levels at 230.1 nm as described in the theory section [32]. This requires a high peak laser intensity. To this end, the frequency doubled output from the Nd:YAG at 532 nm with a pulse energy of 800 mJ is used to pump the dye laser tuned to 587.2 nm at 150 mJ per pulse. The dye laser used Rhodamine 610 dye solved in ethanol. The output of the dye laser was then frequency doubled again to reach 293.6 nm. Finally, the 293.6 nm beam was mixed with the residual 1064 nm beam left after the initial doubling process yielding the desired 230.1 nm. At this stage, the pulse energy had been reduced to a mere 9 mJ.

Using a series of prisms, this beam was then directed towards the reaction cell. Before the cell, the beam was expanded to the desired height of around 6 mm and formed into a thin sheet. This was performed using a concave cylindrical lens (L1 in figure 10) with a focal length of $-4$ cm and a convex lens (L2) with a focal length of 15 cm. The lenses were positioned such that the focus of the beam was in the very centre of the reaction cell. The focal length of the convex lens was chosen such that the beam waist was as long as possible to preserve spatial resolution. At the same time, the beam should not be focused so much that it may incur burn damage at the intersection with the reaction cell windows. An aperture was used to cut the beam to ensure sharp edges. This made it possible to position the beam a very small distance, around 100 µm, above the catalyst surface without any major scattering from the catalyst itself. In order to monitor the energy of the 230 nm beam on a shot-by-shot basis, a power meter was positioned to collect the back re-

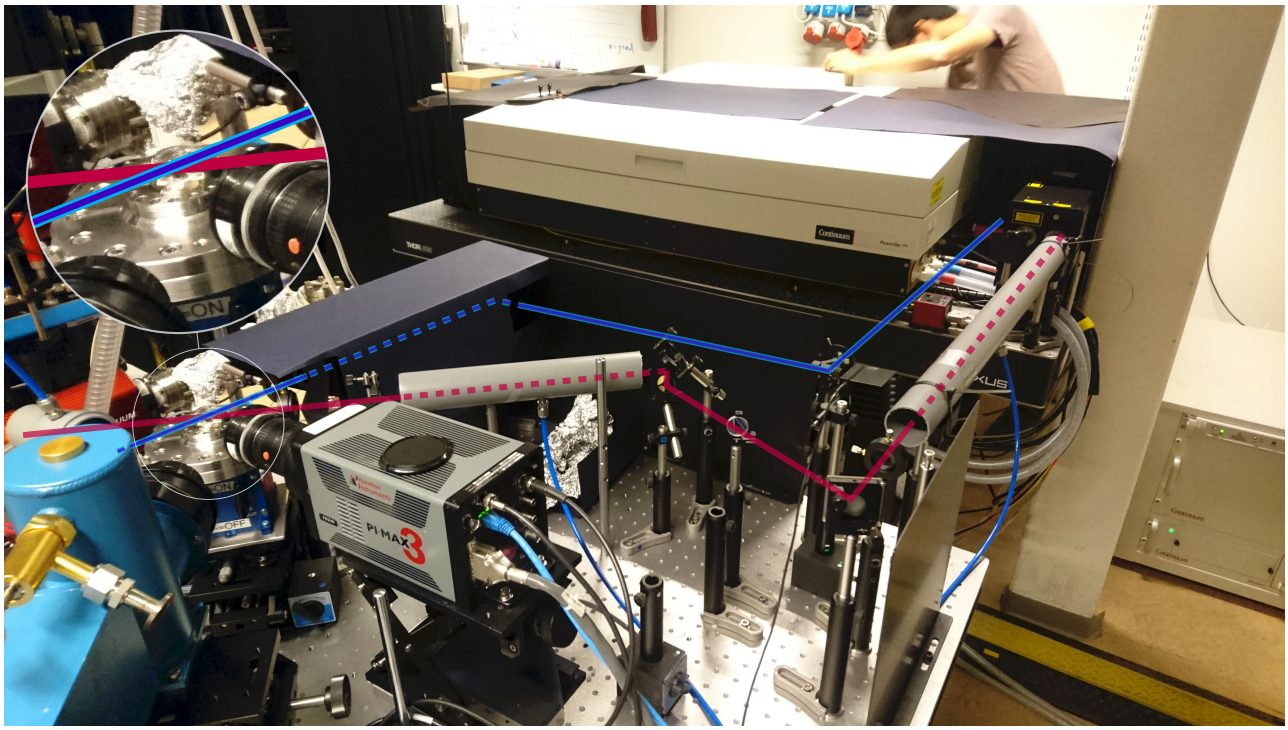


***Figure 11:*** *An annotated photograph of the experimental setup. The 2.7 µm laser (red) originates from the OPO after which it is directed towards the reaction cell. The grey tubes surrounding the beam used to purge the beam with nitrogen gas to lower the absorption as it travels through air. The 230 nm laser (blue) originates from below the cardboard cover. It is then directed to the cell via a series of prisms.*

flection from one of the prisms.

The fluorescence, which was in the visible range as explained in the theory section was imaged by an ICCD camera (Princeton Instruments PIMAX 3) with a resolution of $1024 \times 1024$ pixels. The camera was equipped with a 50 mm Nikon lens with an aperture setting of 1.2 and a 31 mm extension ring. A long pass filter (LP) was placed between the cell and the camera in order to eliminate some of the fluorescence from the fused silica dome itself. $2 \times 2$ binning was employed in order to reach a capture rate of 10 Hz sacrificing spatial resolution for increased temporal resolution. Figure 12 shows single shot image of the CO fluorescence at a pressure of 500 mbar recorded with a simple cell phone camera. Note the orange fluorescence originating from the fused silica dome, the light blue fluorescence from the CO gas and the dark blue fluorescence from the heating cross.

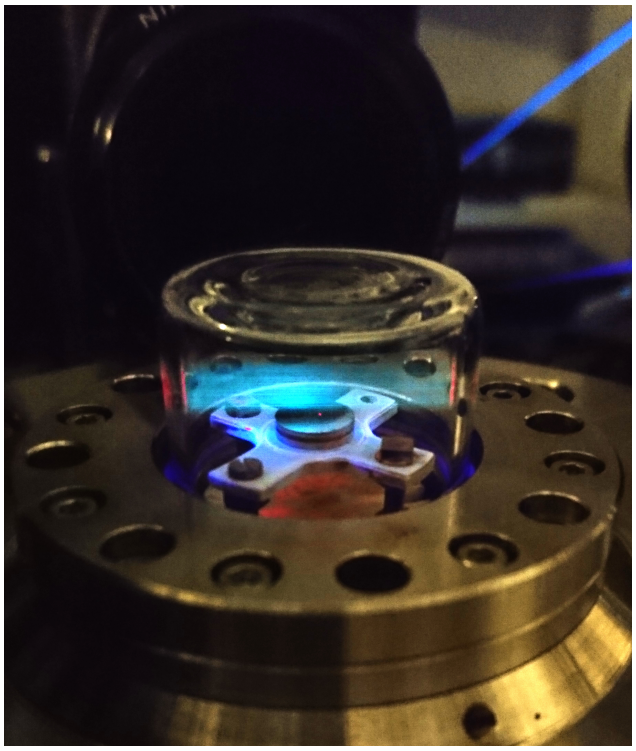

***Figure 12:*** *Photograph of the CO fluorescence using a cell phone camera. The image was taken at 500 mbar pressure with pure CO. Note the different colours for the florescence of the gas (light blue), that from the heating cross (dark blue) and that from the fused silica dome (orange).*

### 3.1.2 Carbon Dioxide Detection

Carbon dioxide ($CO_2$) was detected by exciting the $(00^00) \rightarrow (10^01)$ combination band at 2.7 µm implying mid-infrared. To reach this wavelength, the 1064 nm beam from the Nd:YAG was used to pump an OPO. The pump beam energy is adjusted to around 350 mJ per pulse by adjusting the Q-switch delay, in order not to incur damage to the OPO. An OPO is a device that uses a non-linear crystal to split the incoming pump beam into two outgoing beams; signal and idler where the frequency of the incoming photons is split among those of the two beams. In our case, the frequency of the 1064 nm pump beam is split into a signal beam at around 1.7 µm and an idler at 2.7 µm. By tuning the angle of the non-linear crystal with respect to the incident beam, the ratio between the wavelengths of the outgoing beams may be adjusted to make the idler beam wavelength match the 2.7 µm line. The desired idler beam energy is then 15 mJ per pulse. The spectral width and shape of the OPO idler output is discussed in more detail in the results section. The obtained beam is then directed to the reaction cell via a series of mirrors. Since the beam was quite divergent, a lens with a long focal length of 50 cm (L5 in figure 10) was used to ensure the beam remains focused as it travels towards the reaction cell. Close to the cell, the beam was shaped into a 6 mm high sheet using a cylindrical concave lens (L3) with a focal length of $-4$ cm and a convex lens (L4) with a focal length of 10 cm.

The resulting $CO_2$ fluorescence at 4.26 µm was then imaged using a 2D $256 \times 256$ pixel InSb focal plane array (FPA, Santa Barbara Focalplane SBF-134) detector cooled with liquid nitrogen equipped with a 50 mm $CaF_2$ lens. The detector was triggered with a 10 µs delay to avoid scattering from the laser itself, which is possible due to the generally long lifetimes of IR-transitions at

lower pressures [33]. The detector was, due to the long detection wavelength, inherently sensitive to thermal radiation, which may vary greatly during a measurement run as the catalyst activity or heating cross temperature changes. The camera was therefore triggered at 20 Hz to ensure that every other image is recorded without any fluorescence present [34]. The images without fluorescence were then used as the background measurement for the previous image. An interference filter (IF) centred at 4.26 µm was used to reduce the thermal background which enabled long exposure times of up to 30 µs without incurring sensor saturation.

Since the $CO_2$ absorption lines being probed are quite strong, a large fraction of the beam energy is lost as the beam travels from the OPO to the reaction cell due to the absorption by $CO_2$ contained in air. Water vapour further contributes to this. To counteract the absorption, the laser beam was enclosed in pipes wherever possible. These pipes were then purged with nitrogen which has no absorption lines around 2.7 µm. Over a beam path of around 5 m this improved the obtained signal by a factor of around 1.7.

## 3.2 Reaction Cell

The reaction cell used consisted of a cross shaped boralectric heating element on which the catalyst sample was placed surrounded by a gas tight cover. In order to monitor the temperature of the cross a type D thermocouple was used which was pressed firmly onto the cross with a screw. Previous measurements have shown that at pressures below 250 mbar, the gas temperature just above the sample is very similar to the sample temperature [35]. Moreover, calibrations of the sample temperature when placed at different points on the heating cross have been performed previously [36]. The gas inlet and outlet were on opposite sides and below the cross. Surrounding the cross was either a cubic cover with windows on three sides or a cylindrical dome. The material of the windows or dome was chosen to be highly transmissive at the wavelength used; sapphire or calcium fluoride ($CaF_2$) was used for IR whereas fused silica was used for UV. Figure 12 shows the cell during a CO detection measurement using the fused silica dome.

For the proof-of-concept measurements presented in this thesis, a circular Pd single crystal sample with a polished 100 surface was used.

### 3.2.1 Reference Cell

Both the laser energy and laser wavelength may drift slightly during an experiment due to mode hopping, slight temperature variation or other laser related changes. In order to be able to correct for such changes, a small part of the 2.7 µm beam was fed into a reference cell containing a fixed, known concentration of $CO_2$. The fluorescence from this cell was measured by a point detector. Discrepancies occurring both in the reference cell signal as well as in the data signal could then be attributed to laser fluctuations and corrected for in the post processing. A separate pressure gauge (not shown in figure) was used to monitor the pressure of the reference cell.

## 3.3 Gas Control System

A schematic view of the gas control system used to control the flow of gas though the catalyst reaction and reference cells is shown in figure 13. The gases originated from gas bottles and were fed though mass flow controllers (Bronkhorst EL-FLOW), which regulated the flow of each gas individually. The gas mixture created this way was then fed through the reaction cell. From the cell, the gas was fed past a leak valve (LV, LPM) and through a pressure controller (PC, Bronkhort EL-PRESS), which regulated the total pressure in both reaction and reference cells. A vacuum pump is further used to keep the output of the pressure controller at vacuum (few mbar) at all times.

The leak valve could be opened to leak a small amount of gas into a separate vacuum system connected to a mass spectrometer (MS). A feedback

loop controlled the leak valve and ensured that the pressure in this separate vacuum system was kept at $6 \cdot 10^{-6}$ mbar during measurements.

The mass flow controllers used were accurate down to 2 % of their maximum flow. For CO and $CO_2$, flow controllers with a maximum flow of 50 ml $min^{-1}$ were chosen. For the buffer gas used, Argon, the maximum was instead 200 ml $min^{-1}$.

In order to estimate the pressure in the chamber, the pressures measured by the pressure gauge (PG) before the reaction cell and the pressure measured by the pressure controller are averaged. Previous measurements have shown that this yields sufficiently accurate pressure information [36].

If the reference cell was to be filled, the valves surrounding the reaction cell were closed while those surrounding the reference cell were opened. The pressure controller was then used to control the pressure in the reference cell. Once the reference cell was at the desired pressure, the valves surrounding it were closed to keep the pressure at the desired value.

To be able to quickly evacuate the long tubes connecting the gas bottles to the setup in case of leakage or gas bottle switching, the gas bottles were also connected directly to the vacuum pump via a second series of tubing.

Since CO gas is often polluted with nickel carbonyl, a carbonyl trap (not shown in figure) is connected between the CO gas bottle and the setup.

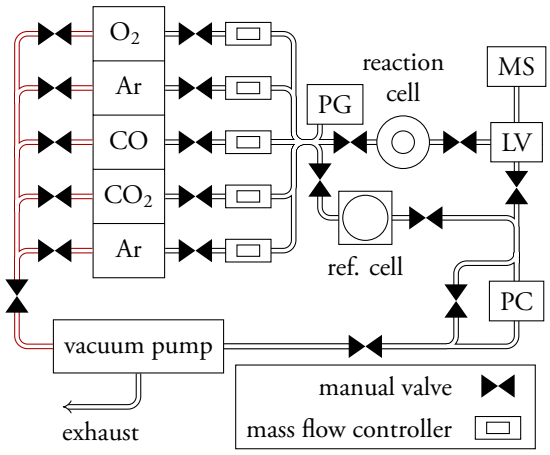


***Figure 13:*** *A schematic view of the gas flow control system part of the experimental setup.*

## 3.4 Measurement

A typical catalyst measurement run consisted of increasing the heating current in order to ramp the temperature of the heating cross from room temperature to a predetermined maximum temperature clearly above the catalyst activation temperature. The heating current itself was regulated by a power supply which was controlled by a LabView program. The current could either be set to simply ramp up at a predetermined pace or be controlled by a PID controller using the thermocouple connected to the heating cross to ensure a linear heating curve.

While the temperature was ramped, the MFCs were set to flow the desired gas mixture through the reaction cell. Most commonly the gas mixture for CO to $CO_2$ oxidation measurements consisted of 4 ml $min^{-1}$ $O_2$, 4 ml $min^{-1}$ CO and 92 ml $min^{-1}$ Ar for a total flow of 100 ml $min^{-1}$. Simultaneously the MS was also measuring global gases concentrations at the gas outlet.

All instruments were controlled and read out continuously during the measurement by a LabView program. Most instruments were read at a rate of 4 Hz while time critical instruments such as the power meter were polled at 10 Hz in order to allow for synchronization with the laser pulses. When measuring $CO_2$, the program also triggered the frame grabber card used for the FPA detector to begin image acquisition in order to synchronize the data images with the instrument data logs. For CO, the image acquisition was initialized manually with as short delay as possible. Usually this delay is under 1 s. However the exact offset was easily determined by comparing the PLIF signal fluctuations to the laser energy recorded by the power meter.

For each set of measurements, a profile dataset was captured at three temperatures distributed

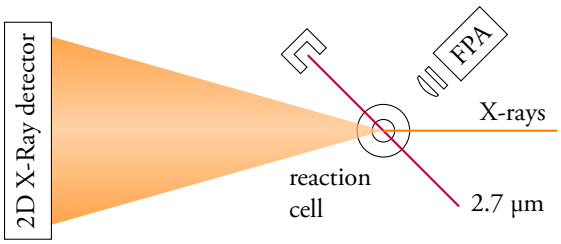


***Figure 14:*** *Top view of the laser and X-Ray arrangement at DESY for performing simultaneous PLIF and SXRD.*

evenly on the temperature ramp used and at a known, fixed gas concentration. This was then used as a compensation for laser sheet inhomogeneity and temperature gradient during post-processing.

In case of CO where the background was static and as such not dependent on temperature, a background measurement was performed to allow for later background subtraction. For this, the laser was tuned away from the CO line, but it was not turned off. This way any scattered light from the laser itself or broad fluorescence from the cell or heating cross was still a part of the background as is desired.

## 3.5 Remote Control

During the thesis work, much time was spent on ensuring that the entire setup can be completely remote controlled from another nearby room. This was necessary for using the PLIF setup in conjunction with SXRD of the catalyst surface performed at a synchrotron facility. Here, humans are not allowed inside the end station hutch for radiation safety reasons [37]. To this end, all controls requiring human manipulation, such as the microscrew controlling the tilting of the OPO crystal, were replaced by motors or circumvented.

## 3.6 Combination of PLIF and SXRD

One of the main purposes of developing a smaller experimental setup was to increase its portability which allows for the possibility to deploy the setup inside a synchrotron beam end station for simultaneous measurements of PLIF and SXRD. In July 2016, we packed the entire experimental setup required for PLIF into a truck and drove it to DESY in Hamburg where a high resolution X-ray diffraction beam line (P07) is available at the PETRA III synchrotron. The aim was to acquire PLIF data in conjunction with an SXRD signal with the ultimate goal to examine self-sustained oscillations on a Pd(100) catalyst during CO oxidation.

The PLIF experiment was set up in a similar way as before, but due to time constraints the reference cell was omitted and only $CO_2$ detection measurements were performed. The cell was positioned in such a way that the X-Ray beam and the laser were separated by around 45°. While the heating cross and dome of the cell used were the same as in the lab in Lund, the chamber itself was a larger UFO shaped version, which provided a separate UHV part giving the possibility to sputter and anneal the catalyst sample to clean its surface from pollutants prior to any measurement. In an attempt to achieve self-sustained catalyst oscillations, the catalyst crystal was first subjected to the sputtering and annealing process. Subsequently, the catalyst temperature was kept fixed to around 0.7 A while the amount of oxygen was varied. This was attempted several times, and self-sustained oscillations were indeed observed on the MS and PLIF. However, as we found out later, the carbonyl trap which was to keep the CO gas free from nickel pollutions did not work properly, which caused the catalyst surface to become polluted before the SXRD could be properly aligned. Thus, self-sustained oscillations were never simultaneously observed with both PLIF and SXRD. However, with the aim to obtain data showing the variation in surface structure by means of SXRD, while a variation in gas composition is observed through PLIF, the catalyst activity was controlled by adjusting the $O_2$ flow. A number of data series exhibiting varying catalysis activity and surface structures were recorded and will be presented

in the results section.

## 3.7 Post Processing

In order to obtain quantitative data from the raw camera images, several post-processing steps were required. Since the steps were very similar for both CO and $CO_2$ images, I will first present the steps involved in the post processing of CO data. I will then discuss the differences between CO and $CO_2$.

The post-processing steps involved in converting the raw CO PLIF images to quantitative data are shown in figure 15. First, the background (b in figure 15) is subtracted from the raw images (a). For CO, a background measurement often consisted of a series of around 250 individual images. These were averaged and the result it subtracted from each raw image. This left images showing only the fluorescence of the laser sheet (c). Depending on the time and spacial resolution requirements, a number of such images were averaged. This way, temporal resolution was sacrificed for an increased signal to noise ratio. Averaging 10 images has shown to often yield good results (e).

Next, the images were divided by profile images (f). This yields image maps of the gas concentration relative to a known profile concentration (g). In order to produce these profile images, three images are acquired a with homogeneous gas concentration at three known temperatures chosen to be at the beginning, middle and end of the temperature ramp. From these three images, a profile for each data image and the corresponding temperature was constructed using linear regression. Hence, the profile division step will compensate for all temperature related signal fluctuations such as thermal depletion of the ground state or the fact that warmer gas consumes more space resulting in lower signal at equal pressure as temperature is increased.

In addition, at this stage the images are cropped to the size of the laser sheet.

Lastly, the entire image is divided through by a column of pixels created by averaging ten columns near the edge of the image on a single shot basis. This is done to remove any stripes in the image created by irregularities in the beam profile (h). In order for this to not alter the overall data values, the mean of the image is kept constant during the division process.

For the case of $CO_2$, every image had its own background taken shortly after the image itself as discussed earlier. Therefore, the background can be subtracted on a per-image basis. Also, the column division step is not performed for $CO_2$ as the cloud is very localised to the catalyst which means very little data are available at the image edge to be used as reference of the sheet profile.

In order to calibrate the concentration scale, every pixel value was multiplied by the gas (CO or $CO_2$) concentration used for the profile images. For this to yield acceptable results it is required that the CO and $CO_2$ concentration dependence is linear with increasing signal. A more detailed discussion regarding the linearity of the pressure dependence will be given in the results section.

The scales of the $x$ and $y$ axes were calibrated by using the known size of the catalyst as reference. If a reference cell signal was available, the total laser sheet intensity in each image is corrected by the reference cell fluorescence intensity for that on a shot-by-shot basis.

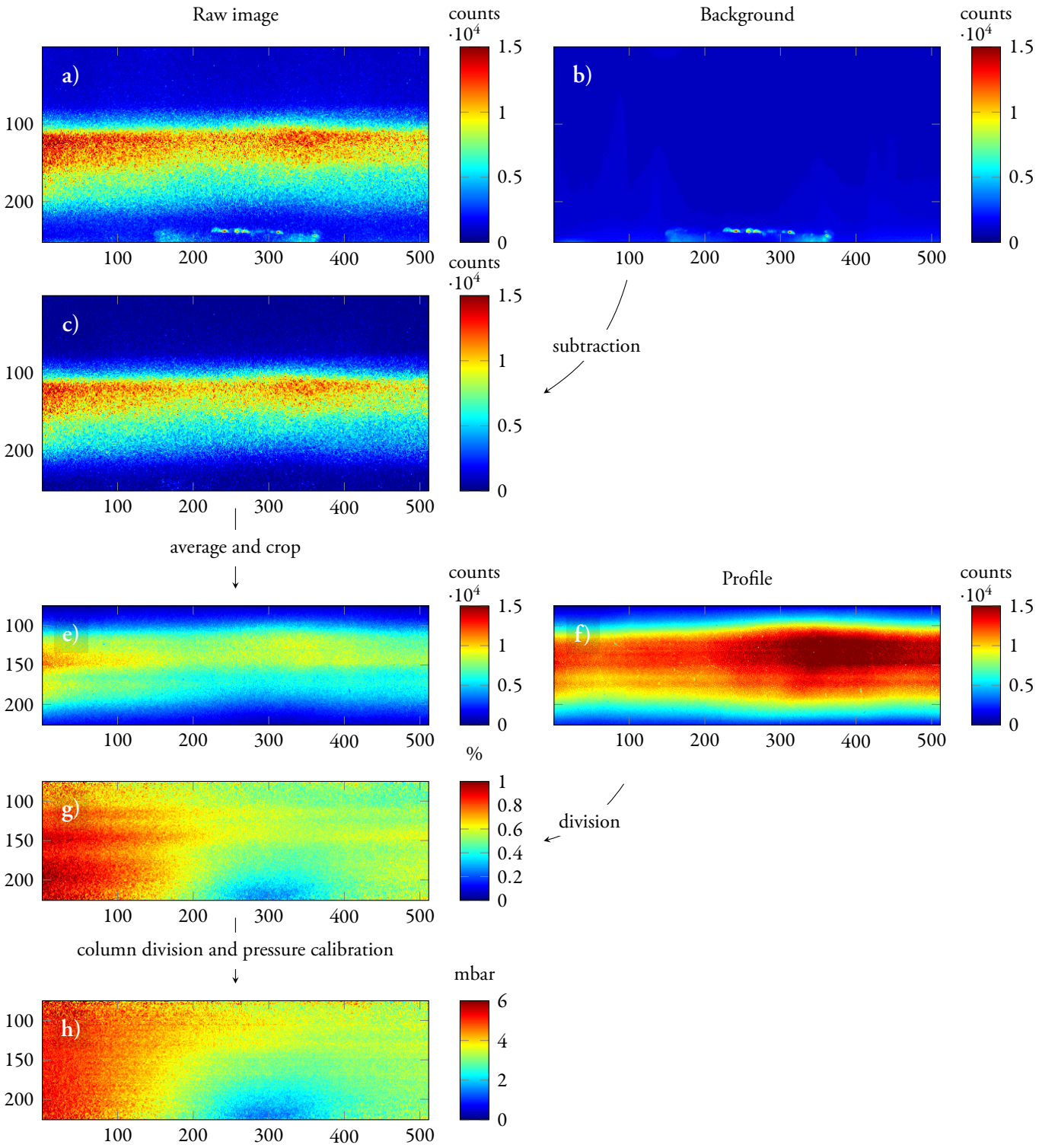


***Figure 15:*** *The post-processing steps involved in producing the data images for CO. All axes indicate pixel numbers. a) and b) show the raw image and background. c) shows the data with the background subtracted. In e), 10 frames such as the one shown in c) are averaged and the image is cropped to only show the laser sheet. g) is the result of e) divided by the profile shown in f). After this step, a "column division" has been performed in h) as outlined in the text.*

# 4 Results and Discussion

In this section the experimental results of importance to this thesis will be presented. First, I intend to present the calibration measurements and discuss the laser line shapes. I will then move on to the proof-of-concept measurements performed using the new setup developed in this thesis. Finally, I will discuss the measurements performed at DESY.

## 4.1 Calibration Measurements

In order to be able to acquire knowledge about the accuracy of the PLIF measurements, concentration dependency measurements were first performed for both CO and $CO_2$. Here, the entire reaction cell was filled with a mixture of CO or $CO_2$ combined with Ar, yielding various CO or $CO_2$ partial pressures at a total pressure of 100 mbar. Subsequently, the PLIF signal was measured at room temperature, an average of 200 frames was used to reduce noise. The results of these measurements are shown in figure 16.

As can be seen, the shapes of the curves are quite different. While the CO signal exhibits a linear dependence on partial pressure, the $CO_2$ signal dependence on partial pressure is clearly not linear as the gain in signal decreases for higher pressures. This effect is mainly attributed to self-absorption of the fluorescence signal which naturally increases with increasing $CO_2$ concentration. If we assume the non-linearity is mainly due to self-absorption, with concentration dependent quenching effects only playing a minor role, we can attempt to fit a function of the type

$$I = c_1 P \mathrm{e}^{-P c_2} \ , \tag{7}$$

where $I$ is the observed LIF intensity, $P$ is the partial $CO_2$ pressure in the reaction cell and $c_1$ and $c_2$ are experimentally determined constants. The first factor represents the increase in signal due to higher $CO_2$ concentration while the second factor represents the decrease of the signal due to self-absorption

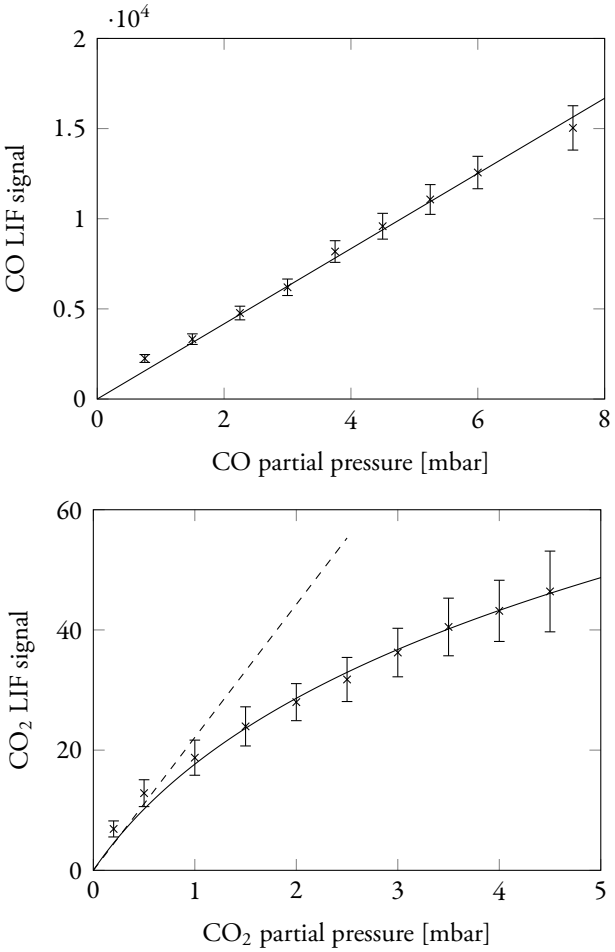


***Figure 16:*** *Pressure dependence measurements for CO and $CO_2$. The dashed line in the $CO_2$ plot corresponds to the signal without any quenching or self-absorption effects which would yield a linear increase of the signal with increasing pressure.*

following the Beer-Lambert law. This function is used in the figure matches the data fairly well. The overall self-absorption effect may seem quite severe, however in actual experiments the fluorescence from $CO_2$ will only pass through the comparatively small cloud of $CO_2$ just above the catalyst. Hence, the path along which self-absorption is possible is much shorter. We thus assume that the contribution of self-absorption effects during catalysis measurements will be small enough to justify a linear pressure dependence also for $CO_2$ as indic-

ated by the dashed line.

For CO, there is no or very little self-absorption as the fluorescence signal does not correspond to a transition involving the ground state but is a transition between two excited states as shown in figure 1. Hence, only the few molecules which are already in the lower excited state can reduce the signal by self-absorption. Moreover, the CO transition is a two-photon transition which further lowers the possibility of self-absorption to occur; the probability of two fluorescence photons interacting at once with a CO molecule is very low at the low intensity the fluorescence exhibits.

The background noise for $CO_2$ is almost non-existent, which yields a low detection limit of 0.1 mbar at a signal to noise ratio of one, despite the lower signal. The corresponding threshold for CO is determined to be 0.5 mbar.

In addition to the partial pressure dependence measurements, excitation scans have been performed for CO and $CO_2$. Here, the respective lasers were scanned over the frequencies relevant to the transitions used for detection of the respective species. For CO, this was accomplished by scanning the dye laser using the built in motors, for $CO_2$ the angle of non-linear crystal inside the OPO was varied using a stepper motor. The result of these scans are shown in figure 17. The CO wavelength axis was calibrated by assuming the peak to be at $2 \times 230.10$ nm as given by literature [32]. On the other hand, the wavelength scale in the $CO_2$ graph was calibrated by aligning the shape of the spectrum to that given by the HITRAN [38] database.

As expected, the $CO_2$ vibrational band being probed is much broader in frequency compared to the CO band. The $CO_2$ spectrum clearly shows the rotational P and R branches for the $10^01$ state at 2690 nm as well and the $02^01$ state at 2770 nm.

With the aim to determine the line shape of the OPO output beam, doppler broadened $CO_2$ lines from the HITRAN database were convoluted with a number of possible laser line shapes. The goal was to determine both the width of the line shape

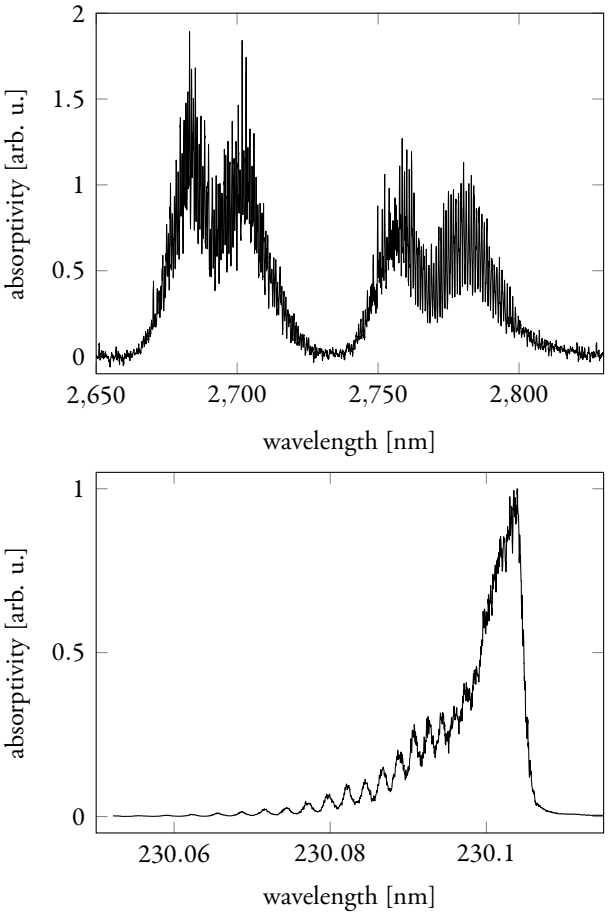


***Figure 17:*** *Excitation scan showing the PLIF intensity while scanning the dye laser or OPO over the frequency region of the relevant transitions.*

envelope as well as any fine structure within. It was found that the OPO spectrum was around 10 $cm^{-1}$ wide. Additionally, the spectrum was found to contain a substructure, the spacing of which is of the order of the rotational lines in the targeted $CO_2$ transitions. This could explain the beating pattern like fluctuations in the scan, which can be most clearly seen at around 2760 nm in figure 17. Moreover, we found that the signal is sensitive to very small adjustments to the OPO crystal angle which could be explained by the OPO spectrum moving in and out of phase with the rotational lines.

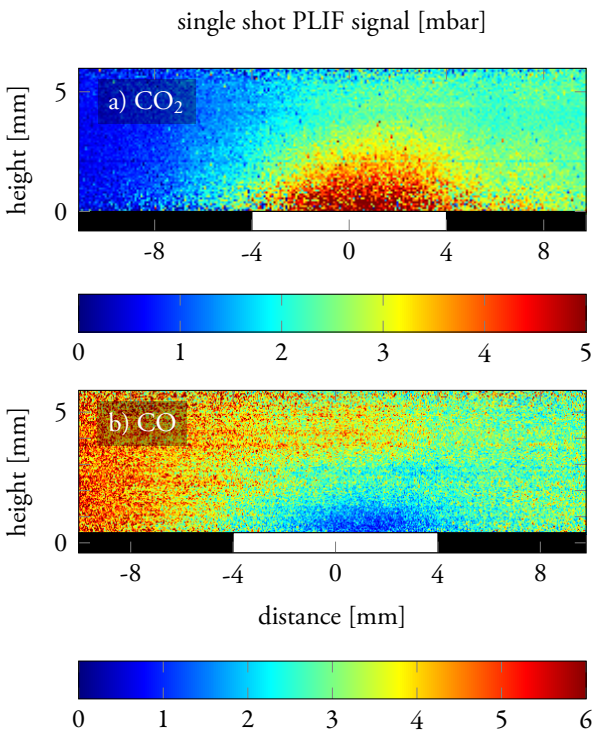


***Figure 18:*** *Single shot data for $CO_2$ (a) and CO (b). These images are from the same dataset that was used to create the images used in figure 19. The images were presented were chosen to be close in time to 19:1c and 2c.*

## 4.2 Proof-of-Concept

In order to investigate the time and spatial resolution of the PLIF setup in a working catalyst scenario, a number of proof-of-concept measurements were performed for both CO and $CO_2$ detection using a Pd(100) single crystal catalyst with a diameter of 8 mm. The result of these measurements is shown in figure 19. Note that all images presented here are the result of 10 shot averaging as part of the post processing. For comparison, single shot images for CO and $CO_2$ are shown in figure 18.

Two consecutive measurements were performed using similar heating current ramps; for CO the heating current was ramped from 0.65 A to 1.15 A, for $CO_2$ it was ramped from 0.60 A to 1.20 A. This results in a slightly larger temperature range for $CO_2$, however any data not within the CO ramp were cut off. This means the temperature range within which data was collected was from 198 °C to 350 °C during which the temperature was increased by 2.9 °C$s^{-1}$. For both gases, the laser sheets were arranged to be perpendicular to the catalyst surface and around 6 mm tall. The bottom of the sheets were around 100 µm above the catalyst surface while the sheet itself was centred above the catalyst (white rectangle).

The measurements were performed at flows of 4 ml $min^{-1}$ $O_2$, 4 ml $min^{-1}$ CO and 92 ml $min^{-1}$ Ar as buffer gas for a total flow of 100 ml $min^{-1}$ at a pressure of 150 mbar. This corresponds to initial partial pressures of 6 mbar for both CO and $O_2$. In figure 19, the panels to the left show the $CO_2$ florescence signal at various activation stages of the catalyst while the panels to the right show the CO signal at equivalent stages. The topmost panel trends the PLIF signal in the regions indicated by the rectangles. The signal recorded by the MS during the $CO_2$ measurement is shown in the panel below; This signal is very similar to that recorded during the CO measurement.

The pressure axes were calibrated by assuming the profile images used to calculate the final concentration images represent 6 mbar partial pressure for the respective gases which was obtained by flowing 4 ml $min^{-1}$ CO or $CO_2$ and 96 ml $min^{-1}$ Ar at 150 mbar.

As the $CO_2$ self-absorption was quite high, and the $CO_2$ profiles were recorded with the entire cell filled with $CO_2$, the profile intensity for that gas will be lowered which might yield an artificially increased $CO_2$ signal when performing the profile division step described in the method section.

For both gases, the images and trends shown were integrated over ten frames giving a temporal resolution of 1 s. By integrating over a smaller number of frames, image quality can be traded for increased temporal resolution. The spatial resolution in the image plane is limited mainly by the detector resolution. In the case of $CO_2$, the laser sheet spans

75 × 256 pixel (the full sensor being 256 × 256 pixel) giving a resolution of 80 µm per pixel. In the case of CO, the sensor had a larger resolution of 1024 × 1024 px. However in order to be able to capture at 10 Hz, 2 × 2 binning had to be used resulting in 40 µm per pixel. In the depth dimension (normal to the image plane), the resolution is given by the thickness of the laser sheet as the vast majority of the fluorescence, with the exception of atoms re-emitting after self-absorption, originates from within the laser sheet. Measuring the exact thickness of the 2.7 µm laser sheet used for IR detection was difficult due to the lack of calibrated burn paper sensitive at that wavelength. Moreover, the beam was not collimated as it leaves the OPO making calculations difficult. However, by using graphite covered cardboard as burn paper to visualize the 2.7 µm laser sheet, it was approximated to be less than 250 µm thick.

The UV laser sheet at 230.1 nm used to visualize the CO had a rather well defined diameter of around 5 mm prior to being focused. Gaussian beam calculations can thus be performed, and yield a sheet thickness of 6 µm.

From a catalysis point of view, the results clearly show the formation of a $CO_2$ cloud above the catalyst as the sample activity increases, with a very sharp increase around the ignition temperature of 317 °C . After ignition, the reaction rate is limited by the diffusion of the reaction components to and from the surface, the so-called mass transfer limit [39], which results in the respective trends levelling out. Since the molar amount of $CO_2$ produced must correspond to the molar amount of CO missing, it would be expected that the results reflect this. As can be deduced from the plots, the CO concentration drops from 6.2 mbar to 1.6 mbar, a drop of 4.6 mbar. The $CO_2$ concentration on the other hand rises from zero to around 4.4 mbar. When comparing the shape of the CO and $CO_2$ clouds, they rather clearly look like each others inverse, further validating the accuracy of the method. Hence, the current method does seem to provide accurate results.

However, there are several possible sources of error worth discussing. First, there may be a slight drift of the laser in both energy and wavelength during a measurement or between the capture of the profile images and the measurement itself. As shown in figure 20, this drift while slow may be large over time. It was attempted to use the reference cell to control for these fluctuations as discussed in the method section, but the low signal of the reference cell resulted in a very low signal-to-noise ratio, rendering it unusable. While it would be possible direct to a larger fraction of the beam energy into the reference cell, increasing the reference signal, this would in turn lower the energy of the beam in the reaction cell decreasing the signal-to-noise ratio of the PLIF images. A similar dilemma is faced regarding an accurate power measurement; if the wavelength drift is smaller the absorption in the air will be increased, which decreases the measured power while the signal might even increase. These two problems make it very difficult to accurately compensate the signal for wavelength and energy drifts.

We currently alleviate the issues discussed above by aqcuiring a large number of profile datasets during a measurement campaign which ensure that profile data recoded close in time are available for all measurements. However, this is clearly inconvenient and not always possible as discussed in the next section presenting the DESY results.

Another source of error is the quenching effect discussed in the theory section, where molecules excited by the laser beam de-excite by ways other than direct photon emission. This is mainly an issue because the extent of signal loss due to quenching for detection of a species not only depends on the concentration of that species, which would yield a simple linear contribution. Instead, it also depends on the concentration of other species. In this case, the quenching of the $CO_2$ signal depends on the concentration of $CO_2$, CO and $O_2$. Measurements have revealed that, while the effect from $O_2$ is low, the CO concentration has a large effect on the

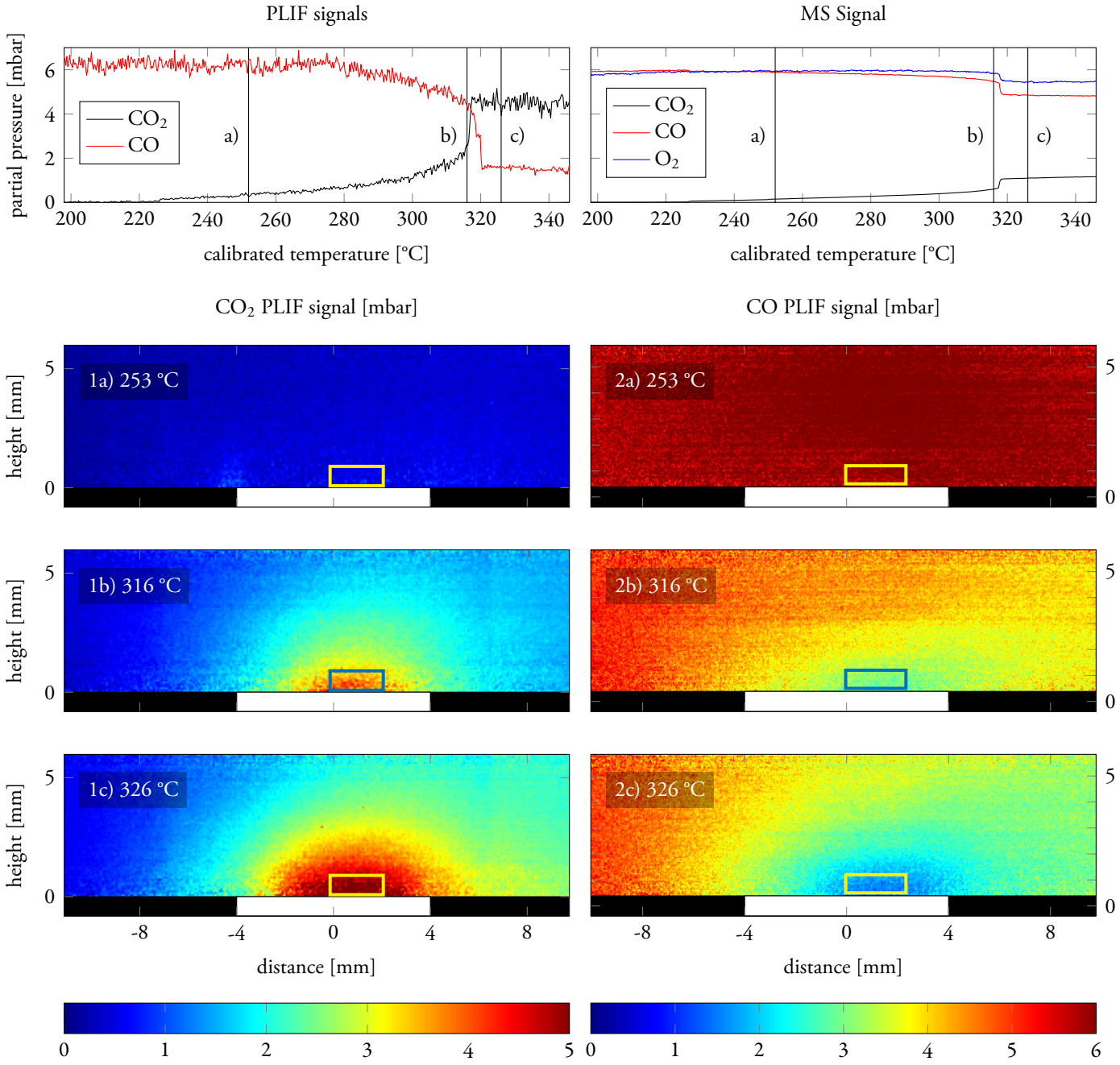


***Figure 19:*** *PLIF data showing the oxidation of CO to $CO_2$ using a Pd(100) single crystal catalyst. Two measurements were performed consecutively using similar temperature ramps. Panels 1a-1c to the left show the $CO_2$ signal while panels 2a-2c CO signal. Adjacent images are taken at similar temperatures corresponding to similar catalyst activity as shown in the trend plots. The topmost panels show the average PLIF signal in the rectangles just above the catalyst and the signal from the MS which analyses the gas leaving the reactor.*

$CO_2$ signal. In fact, at 6 mbar of CO in addition to 6 mbar $CO_2$ and 138 mbar Ar, the $CO_2$ signal was reduced by around 25 %. This effect should not have a large influence on the measured $CO_2$ concentration near the active catalyst surface, due to the low amount of CO present there. However, quenching will result in an underestimation of the $CO_2$ concentration in areas where CO is present to a large extent which leads to a misjudgement of the shape of the cloud gradient as well as an underestimation of the $CO_2$ concentration above the not yet ignited catalyst.

Regarding the effect of quenching on the CO signal, measurements have shown a decrease of around 12 % when 6 mbar of $CO_2$ are present. Hence, in areas where the CO presence is low, the concentration may be underestimated.

Currently, quenching effects are not corrected for as there currently are too little data available to accurately take the effect into account in the concentration maps. However, when more in-depth measurements of the quenching effects are performed, it will be possible to incorporate the results of these into the creation of the concentration maps.

A manuscript that treats the experimental setup and presents the proof-of-concept data presented in this section, has been submitted to Applied Physics B [40].

## 4.3 DESY

At DESY, simultaneous measurements combining PLIF and SXRD were successfully performed. For the first time, is has been possible to simultaneously aquire both SXRD data representing the surface structure of a working catalyst, and PLIF data visualizing the surrounding gas.

As outlined in the methods section, the ultimate goal of acquiring data while observing self-sustained oscillations was not yet achieved. Instead, periodic fluctuations in catalyst activity were archived by cutting off the flow of oxygen during catalyst activity. Clear correlations between variations in surface structure shown by the SXRD signal, and varying gas concentrations as shown by the PLIF signal, were observed.

The resulting data are shown in figures 21 and 22. The PLIF images and corresponding XRD diffraction patterns were recorded within 250 ms of each other, as SXRD data were aquired at a rate of 2 Hz while five raw PLIF images were averaged to also yield 2 Hz. The trend plots in figures 21 and 22 show the average $CO_2$ concentration close to the catalyst (blue rectangle) as determined by PLIF; the times at which the images were recorded are also indicated.

Prior to the oxygen being cut at around 825 s as shown in figure 21, the catalyst had been active for a few minutes, during which a polycrystalline oxide film have formed on the surface, as is evident from the circular lines in the diffraction patterns (21:1a-1f). As the oxygen was cut, this oxide layer was no longer stable and dissolved. This process occurred simultaneously to the decrease in reaction products in the gas above the catalyst as indicated by the simultaneously acquired PLIF signal (21:2a-2f). Figure 22 shows images recorded when cutting the oxygen a second time. However, this time the catalyst had only been active for a short while as indicated by the trend plot. Consequently, no polycrystalline oxide has yet formed. Instead, CTRs attributed to oxygen adsorbed directly to the surface are visible as indicated by the yellow arrows. As expected, these disappeared synchronously to the drop in catalyst activity as the flow of oxygen was cut.

We speculate that if conditions are such that the catalyst is highly active, a polycrystalline oxide would begin to grow on the surface. Once the oxide has grown to a certain theshold thickness, the topmost layers of the oxide no longer feel any potential from the substrate, which causes them to arrange in their preferred crystal structure. This new crystal structure no longer exhibits as many catalytically active sites, which causes a subsequent drop

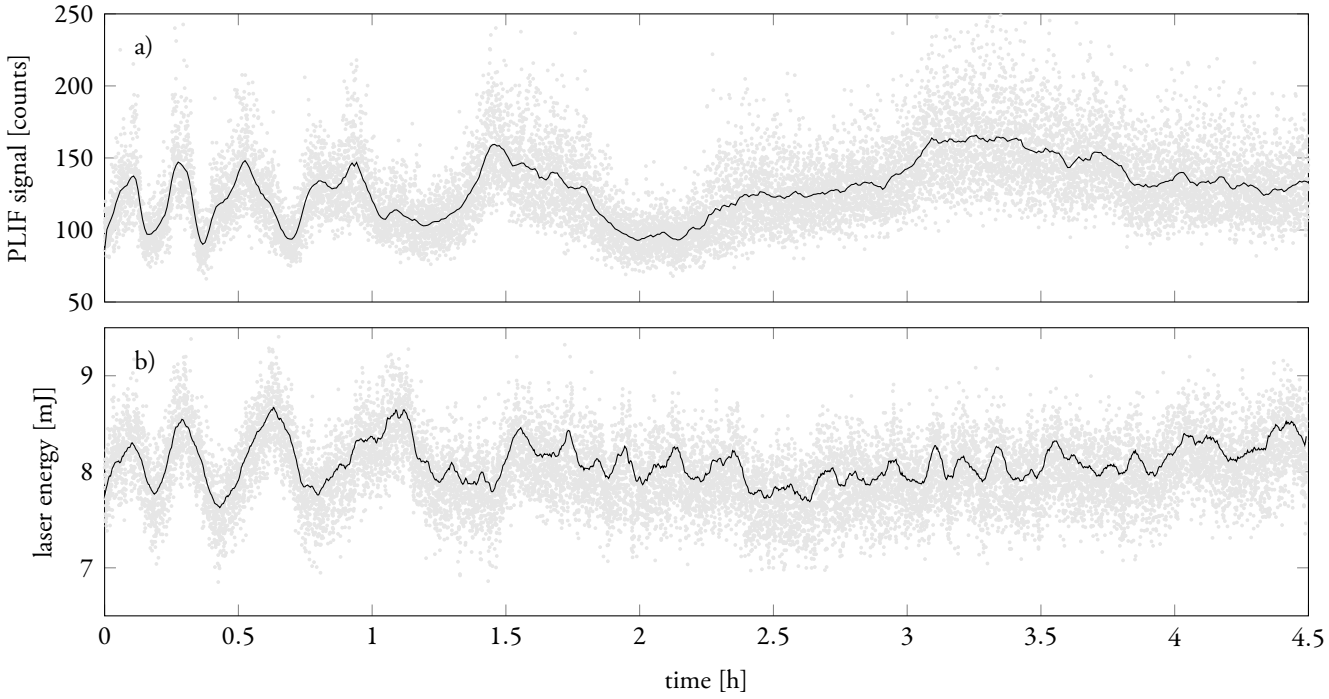


***Figure 20:*** *The PLIF signal fluctuations (a) and laser energy fluctuations (b) over time while keeping a constant 3 mbar of $CO_2$ in the reaction cell. The power meter was positioned behind the reaction cell.*

in catalyst activity. There will however still be CO in the surrounding gas which will reduce the oxide. Once the oxide has been reduced, the surface will be rough, as the Pd left from the reduced oxide will be distributed unevenly. This type of surface is not highly active at lower temperatures as the reaction products will be more tightly bound to the surface resulting in fewer active sites. Over time the surface would flatten, returning the surface to its original state which would restart the cycle.

During the experiment, nickel pollutions may have caused an increased surface roughness and fewer active sites which increased the threshold temperature to reach the highly active phase. Once in this phase, the higher temperature caused the polycrystalline oxide to also be active. Consequently, no self-sustained oscillations could arise.

As this was the first time PLIF and SXRD were combined to measure the properties of a working catalyst, some shortcomings in the current PLIF setup were found. First, the PLIF setup was designed to measure catalyst activity while the catalyst temperature was altered, and with gas flows kept constant. As mentioned, this turned out to be problematic for the SXRD measurement, as variations in temperature cause the surface to shift outside of focus. A system, where the gas flow can be ramped would be more suitable. Second, currently the way in which the acquisition and post-processing procedures are set up does not allow to continuously acquire data for a longer period of time and perform the subsequent analysis steps on only a subset of the data. Such arrangement would be convenient in a scenario where one is waiting an event to occur instead as opposed to simply investigating catalyst activity during a pre-defined timespan. Furthermore, certain catalyst measurement procedures require a fixed gas concentrations and temperature for a longer period of time which renders frequent profile measurements impossible. This intensified the presented issues regarding the drift of the laser wavelength and energy.

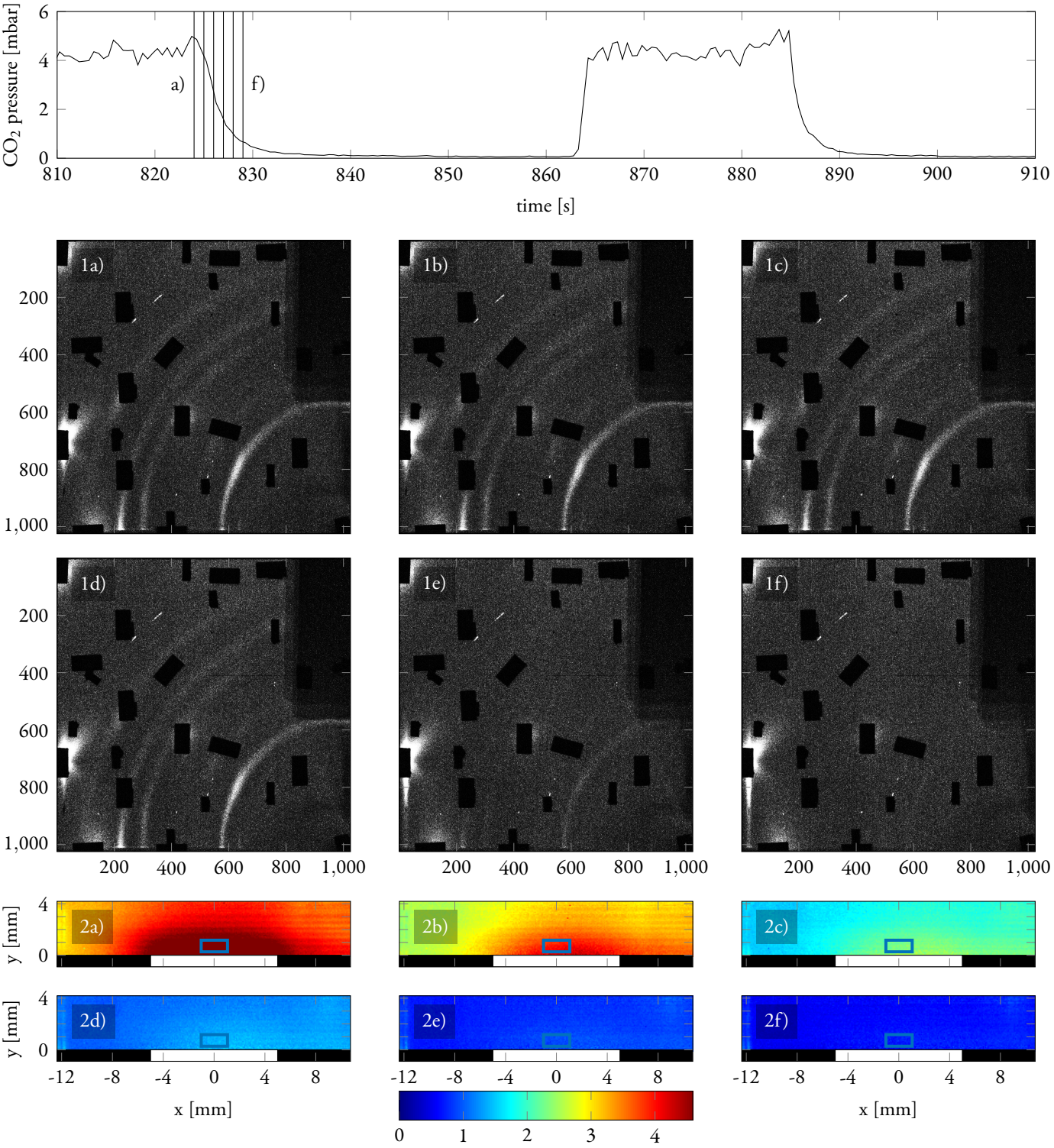


***Figure 21:*** *A series of images showing PLIF data (2a-2f) and simultaneously acquired SXRD diffraction patterns (1a-1f). The very top panel trends the average PLIF signal in the blue rectangles. The images are acquired while the oxygen flow to the reaction was throttled resulting in a stagnation of catalyst activity. Simultaneously, the circular diffraction pattern, which is attributed to bulk oxide on the catalyst surface, also disappears.*

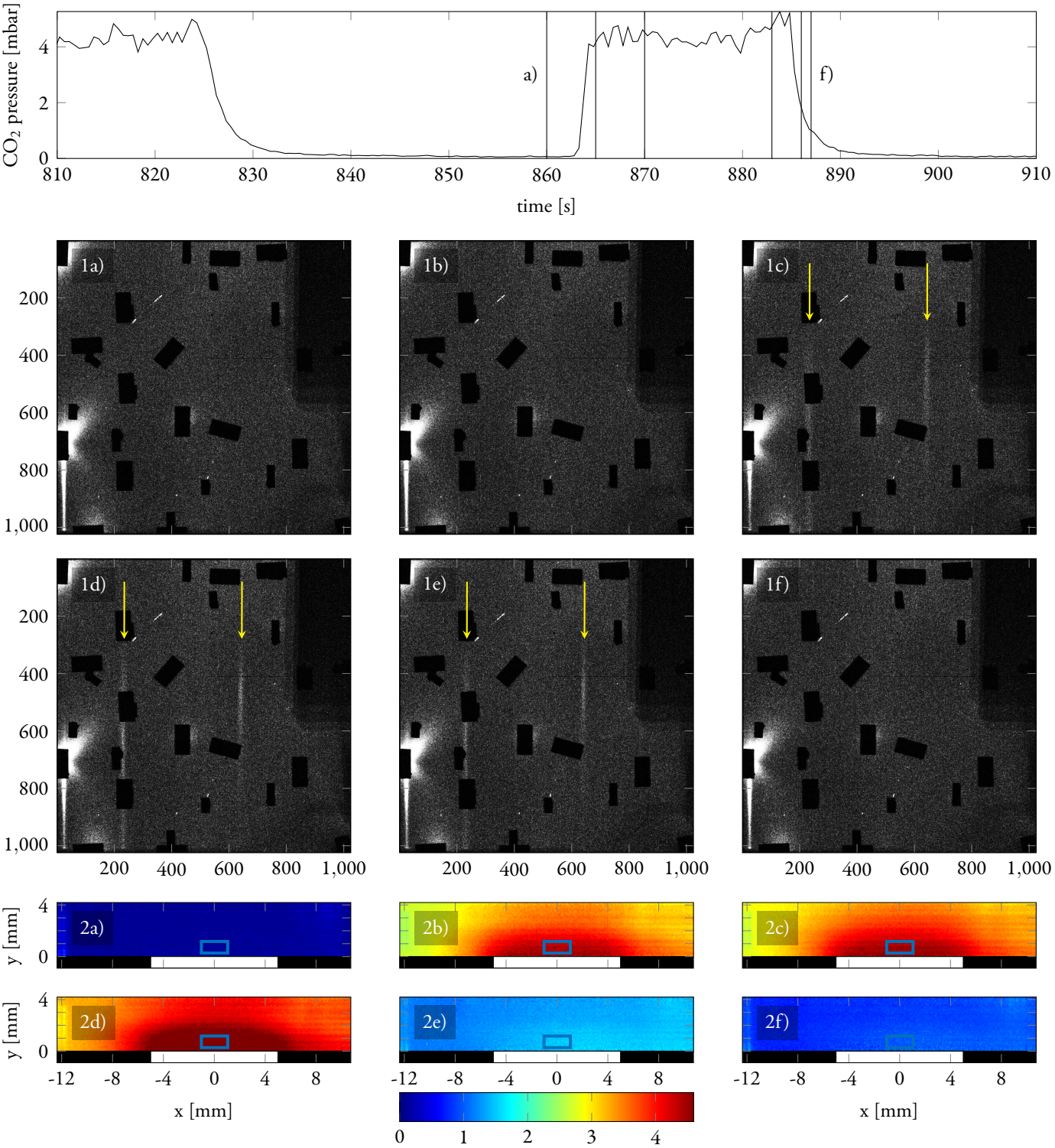


***Figure 22:*** *A series of images showing PLIF data (2a-2f) and simultaneously acquired SXRD diffraction patterns (1a-1f). The very top panel trends the average PLIF signal in the blue rectangles. The images are acquired while the oxygen flow to the reaction was increased and then throttled resulting in an increase followed by a stagnation of catalyst activity. Simultaneously, the CTRs (yellow arrows), which are attributed to oxide on the catalyst surface, also appear and disappear.*

# 5 Conclusion

We have successfully developed a convenient experimental setup for *in situ* detection of CO and $CO_2$ using PLIF that can be used to create two-dimensional images of the gas distribution around a working catalyst. With low detection limits, especially for $CO_2$, and high spatial resolutions, we are certain this technique will be an invaluable tool for catalysis studies.

This setup was then taken to DESY, where PLIF and SXRD signals could be simultaneously acquired. We have shown that there is an clear correlation between surface structure and catalyst activity, by comparing contemporaneous images of the gas distribution aquired by means of PLIF with the SXRD signal. We have thus proven that the combination of SXRD and PLIF is not only possible, but also feasible to do in the very limited time window provided by a synchrotron beamtime slot.

Compared to MS, which is the commonly used technique for gas detection, PLIF has several advantages. First, PLIF is a non-intrusive technique which does not in any way affect the gas flow or the chemical reactions that occur. Second, PLIF measures the gas concentrations *in situ* which results in no delay between the situation to be probed and the acquired data. MS data will always be delayed since it takes time for the gas to travel from the probe inlet to the analysing apparatus. Third, PLIF yields two-dimensional images of the probed distribution. The creation of two-dimensional images is possible with MS, given that several probes are used or by consecutive measurements in which the probe position is altered. However, spatial resolutions will be very low and the procedure makes it difficult to not affect the gas flow. Furthermore, with MS, a tradeoff between a more intrusive measurement close to the catalyst surface, which will probe the gas concentration near the catalyst more accurately, and a measurement of the average gas concentration in the reactor with little regard to the exact concentration at the catalyst must be made. Finally, another issue with MS is that it is difficult to distinguish between species of the same mass. This is especially worrisome when detecting CO, as it has the same weight as nitrogen, which is abundant in air and might leak into the system.

When using MS, one does however, enjoy several advantages when compared with PLIF. First, MS systems are much smaller and can be easily transported and implemented into existing reactor configurations. In addition, a single MS analyser can detect several gas species at once, something which is more difficult with PLIF. Ideally, both PLIF is used together with an MS connected to the gas outlet as is the case in this work. This way, the advantages of MS, such as multiple species detection, are combined with the two-dimensional imaging capabilities and *in situ* properties of PLIF, without the need of probes that affect the gas flow in the reactor.

# 6 Outlook

When discussing further improvements and expansions to this work, one has to differentiate between improvements to the method itself and applications. Regarding improvements of the method, many more reference measurements could be performed to further investigate issues such as quenching or self-absorption, and find possibilities to accurately correct for such issues. It would also be helpful to find a reliable solution to correct for short term and long term energy and wavelength drifts. One possible solution to accurately measure the pulse energy would be to perform that measurement before the beam enters the OPO, which would render it immune to air absorption issues. However, this method would require the energy of the 1064 nm beam prior to the OPO to be proportional to that of the 2.7 µm beam, which has not been confirmed.

This method will also not take wavelength drifts into account, which may have a large effect on the signal intensity. As such, it will be important to further develop the reference cell and the accompanying optics to increase the reference cell signal to a usable level. Measurements, in which varying fractions of the beam are directed to the reference cell could be performed to find a good compromise between reference cell and reaction cell signal intensities. Nonetheless, a measurement of the "raw" laser energy output would be useful to decouple fluctuations introduced by the OPO with those caused by the laser itself.

Moreover, it is planned to attempt pumping the OPO using the residual 1064 nm beam left after the mixing process. If successful, it would enable simultaneous measurements of both the CO and $CO_2$ concentrations. However the beam quality of the 1064 nm after mixing will be very bad which probably will result in poor OPO performance making this attempt diffucult.

Regarding CO measurement, it would be interesting to attempt to measure the flourescence signal with a regular Digital single-lens reflex (DSLR) camera with a Complementary Metal Oxide Semiconductor (CMOS) sensor. While this type of cameras does not allow for gating or signal intensification or binning, the cameras are much cheaper as they are mass produced, which motivates the attempt. It would also be sensible to perform tests with non-intensified CCD devices. These are more expensive than CMOS based cameras, but allow for binning and the cost is still much less than that of an ICCD camera.

Another possibility is the use of vibrational IR transitions to detect CO, which would be tuned using the OPO, similar how the $CO_2$ detection is configured in this thesis. Even if it was difficult to combine with $CO_2$ measurements as mentioned in the theory section, another method of measuring CO could be used to validate the UV-based results.

Furthermore, a better organisation and automation of the post-processing would be beneficial. Especially if additional parameters and corrections are to be taken into account, a more organised system to handle and analyse the data will be invaluable. Further development on the software side will be necessary to achieve this. The shortcomings regarding acquisition cycle length and the now lacking possibility to ramp gas flows, which were mentioned earlier, also fall into the software category.

Regarding the temperature measurements, one could attempt to extract temperature data from $CO_2$ background images. While these only image the side of the catalyst, which is out of focus, it might be possible to use the images in conjunction with thermocouple data to further improve the accuracy of the temperature data.

On the application side, there is a near infinite number of possibilities given the large number of catalyst-gas combinations available. For example $NO_x$ is a major pollutant which is detectable using the same setup by probing in the UV regime.

Furthermore, another trip to DESY for further simultaneous studies of PLIF and SXRD is warranted given that the principle worked successfully.

# 7 Acknowledgements

I would first and foremost like to thank my supervisor **Johan Zetterberg** for his encouragement and trust and patience. I truly appreciate the insight you have given me into academia and the many thoughts and suggestions you provided during the work with this thesis.

Furthermore, I would like to express my sincere thanks to **Jianfeng Zhou** who I spent a great deal of time with. Jianfeng's willingness and patience to explain things, sometimes over and over, is something I really appreciate. The many discussions we had during our many lunches together were also very enlightening and helpful. This thesis would not be nearly as thought through without him.

I would also like to thank **Mikhail Shipilin** for a great time at DESY and a very helpful explanation of SXRD in his thesis, it was very clearly written and a great help when compiling the theory section of this thesis. Moreover, I would like to thank **Sara Blomberg** for her always very encouraging words, every time I met her. I also really appreciated the help of the DESY staff, **Olof Gutuwski** and **Uta Ruett** for their help during the rather tiresome, but on the other hand fantastic, campaign week. Finally, I would like to thank **Johan Gustafsson** for taking his time to explain the more quirky bits with catalysis, and also for proof-reading those parts of the thesis.

# References


[1] J. J. Berzelius, *Årsberättelse om framstegen i fysik och kemi*. Norstedt, 1835.

[2] B. Lindström and L. J. Pettersson, "A brief history of catalysis," *CatTech*, vol. 7, no. 4, pp. 130–138, 2003.

[3] G. Ertl, H. Knözinger, F. Schüth, and J. Weitkamp, *Handbook of heterogeneous catalysis: 8 volumes*. wiley-vch, 2008.

[4] S. T. Microscopy III, "Theory of stm and related scanning probe methods," 1993.

[5] J. F. Watts and J. Wolstenholme, *An Introduction to Surface Analysis by XPS and AES*. May 2003.

[6] R. Diehl, J. Ledieu, N. Ferralis, A. Szmodis, and R. McGrath, "Low-energy electron diffraction from quasicrystal surfaces," *Journal of Physics: Condensed Matter*, vol. 15, no. 3, p. R63, 2003.

[7] S. Blomberg, M. J. Hoffmann, J. Gustafson, N. M. Martin, V. R. Fernandes, A. Borg, Z. Liu, R. Chang, S. Matera, K. Reuter, and E. Lundgren, "*In Situ* x-ray photoelectron spectroscopy of model catalysts: At the edge of the gap," *Phys. Rev. Lett.*, vol. 110, p. 117601, Mar 2013.

[8] M. E. Grass, P. G. Karlsson, F. Aksoy, M. Lundqvist, B. Wannberg, B. S. Mun, Z. Hussain, and Z. Liu, "New ambient pressure photoemission endstation at advanced light source beamline 9.3. 2," *Review of Scientific Instruments*, vol. 81, no. 5, p. 053106, 2010.

[9] P. Rasmussen, B. Hendriksen, H. Zeijlemaker, H. Ficke, and J. Frenken, "The "reactor stm": A scanning tunneling microscope for investigation of catalytic surfaces at semi-industrial reaction conditions," *Review of scientific instruments*, vol. 69, no. 11, pp. 3879–3884, 1998.

[10] B. Hendriksen and J. Frenken, "Co oxidation on pt (110): scanning tunneling microscopy inside a high-pressure flow reactor," *Physical Review Letters*, vol. 89, no. 4, p. 046101, 2002.

[11] J. Gustafson, M. Shipilin, C. Zhang, A. Stierle, U. Hejral, U. Ruett, O. Gutowski, P.-A. Carlsson, M. Skoglundh, and E. Lundgren, "High-energy surface x-ray diffraction for fast surface structure determination," *Science*, vol. 343, no. 6172, pp. 758–761, 2014.

[12] R. W. Sidwell, H. Zhu, R. J. Kee, D. T. Wickham, C. Schell, and G. S. Jackson, "Catalytic combustion of premixed methane/air on a palladium-substituted hexaluminate stagnation surface," *Proceedings of the Combustion Institute*, vol. 29, no. 1, pp. 1013–1020, 2002.

[13] K. Kohse-Höinghaus, "Laser techniques for the quantitative detection of reactive intermediates in combustion systems," *Progress in Energy and Combustion Science*, vol. 20, no. 3, pp. 203–279, 1994.

[14] A. C. Eckbreth, *Laser diagnostics for combustion temperature and species*, vol. 3. CRC Press, 1996.

[15] E. Fridell, U. Westblom, M. Aldén, and A. Rosén, "Spatially resolved laser-induced fluorescence imaging of OH produced in the oxidation of hydrogen on platinum," *Journal of Catalysis*, vol. 128, no. 1, pp. 92–98, 1991.

[16] E. Fridell, A. Rosen, and B. Kasemo, "A laser-induced fluorescence study of OH desorption from pt in $H_2O/O_2$ and $H_2O/H_2$ mixtures," *Langmuir*, vol. 10, no. 3, pp. 699–708, 1994.

[17] F. Gudmundson, J. Persson, M. Försth, F. Behrendt, B. Kasemo, and A. Rosén, "OH

gas phase chemistry outside a Pt catalyst," *Journal of Catalysis*, vol. 179, no. 2, pp. 420–430, 1998.

[18] F. Gudmundson, E. Fridell, A. Rosen, and B. Kasemo, "Evaluation of hydroxyl desorption rates from platinum using spatially resolved imaging of laser-induced fluorescence," *The Journal of Physical Chemistry*, vol. 97, no. 49, pp. 12828–12834, 1993.

[19] J. Zetterberg, S. Blomberg, J. Gustafson, J. Evertsson, J. Zhou, E. C. Adams, P.-A. Carlsson, M. Aldén, and E. Lundgren, "Spatially and temporally resolved gas distributions around heterogeneous catalysts using infrared planar laser-induced fluorescence," *Nature communications*, vol. 6, 2015.

[20] S. Blomberg, J. Zhou, J. Gustafson, J. Zetterberg, and E. Lundgren, "2d and 3d imaging of the gas phase close to an operating model catalyst by planar laser induced fluorescence," *Journal of Physics: Condensed Matter*, vol. 28, no. 45, p. 453002, 2016.

[21] B. E. Saleh, M. C. Teich, and B. E. Saleh, *Fundamentals of Photonics, Second Edition*. Wiley New York, 2006.

[22] S. Svanberg, *Atomic and Molecular Spectroscopy: Basic Aspects and Practical Applications*. Springer: Berlin, 2004.

[23] G. Herzberg and K. Huber, *Molecular Spectra and Molecular Structure: Constants of diatomic molecules*. Molecular Spectra and Molecular Structure, Van Nostrand Reinhold, 1979.

[24] M. Born and R. Oppenheimer, "Zur quantentheorie der molekeln," *Annalen der Physik*, vol. 389, no. 20, pp. 457–484, 1927.

[25] B. J. Kirby and B. K. Hanson, "Imaging of CO and $CO_2$ using infrared planar laser-induced fluorescence," *Proceedings of the Combustion Institute*, vol. 28, no. 1, pp. 253–259, 2000.

[26] J. L. Kinsey, "Laser-induced fluorescence," *Annual Review of Physical Chemistry*, vol. 28, no. 1, pp. 349–372, 1977.

[27] A. Beer, "Bestimmung der absorption des rothen lichts in farbigen flüssigkeiten," *Annalen der Physik*, vol. 162, no. 5, pp. 78–88, 1852.

[28] J. Lennard-Jones, "Processes of adsorption and diffusion on solid surfaces," *Transactions of the Faraday Society*, vol. 28, pp. 333–359, 1932.

[29] W. Miller, *A Treatise on Crystallography*. For J. & J. J. Deighton, 1839.

[30] P. Ewald, "Zur theorie der interferenzen der röntgenstrahlen," *Phys. Z*, vol. 14, pp. 465–472, 1913.

[31] M. Shipilin, *Surface Structure and Catalytic Activity of Pd and Fe Oxide Surfaces and Thin Films*. PhD thesis, Lund University, 2016.

[32] M. Aldén, S. Wallin, and W. Wendt, "Applications of two-photon absorption for detection of co in combustion gases," *Applied Physics B*, vol. 33, no. 4, pp. 205–208, 1984.

[33] W. Rosser Jr, R. Sharma, and E. Gerry, "Deactivation of vibrationally excited carbon dioxide (001) by collisions with carbon monoxide," *The Journal of Chemical Physics*, vol. 54, no. 3, pp. 1196–1205, 1971.

[34] J. Zetterberg, S. Blomberg, J. Gustafson, Z. Sun, Z. Li, E. Lundgren, and M. Aldén, "An in situ set up for the detection of co2 from catalytic co oxidation by using planar laser-induced fluorescence," *Review of Scientific Instruments*, vol. 83, no. 5, p. 053104, 2012.

[35] S. Pfaff, "Imaging of the temperature distribution in a catalyst test chamber using laser rayleigh scattering," 2015. Bachelor's Thesis, Lund University.

[36] H. Karlsson, "Calibration measurements in a catalysis reaction chamber using thermographic phosphors," 2015. Bachelor's Thesis, Lund University.

[37] G. Freeman, *Observation of Einstein-Podolsky-Rosen Entanglement on Supraquantum Structures by Induction Through Nonlinear Transuranic Crystal of Extremely Long Wavelength (ELW) Pulse from Mode-Locked Source Array*. PhD thesis, Massachusetts Institute of Technology, 1993.

[38] L. S. Rothman, I. E. Gordon, Y. Babikov, A. Barbe, D. C. Benner, P. F. Bernath, M. Birk, L. Bizzocchi, V. Boudon, L. R. Brown, A. Campargue, K. Chance, E. A. Cohen, L. H. Coudert, V. M. Devi, B. J. Drouin, A. Fayt, J.-M. Flaud, R. R. Gamache, J. J. Harrison, J.-M. Hartmann, C. Hill, J. T. Hodges, D. Jacquemart, A. Jolly, J. Lamouroux, R. J. LeRoy, G. Li, D. A. Long, O. Lyulin, C. Mackie, S. T. Massie, S. Mikhailenko, H. S. Müller, O. Naumenko, A. Nikitin, J. Orphal, V. I. Perevalov, A. Perrin, E. R. Polovtseva, C. Richard, M. A. H. Smith, E. Starikova, K. Sung, S. Tashkun, J. Tennyson, G. C. Toon, V. G. Tyuterev, and G. Wagner, "The hitran 2012 molecular spectroscopic database," *Journal of Quantitative Spectroscopy and Radiative Transfer*, vol. 130, pp. 4–50, 2013.

[39] S. Matera and K. Reuter, "Transport limitations and bistability for in situ co oxidation at ruo 2 (110): First-principles based multiscale modeling," *Physical Review B*, vol. 82, no. 8, p. 085446, 2010.

[40] J. Zhou, S. Pfaff, E. Lundgren, and J. Zetterberg, "A convenient setup for laser-induced fluorescence imaging of both CO and $CO_2$ during catalytic CO oxidation," *Applied Physics B*, 2016. Manuscript submitted.